Electronic Supplementary Information

Visualizing dynamic competitive reconstruction of trimetallic hybrid catalysts for stable hybrid water electrolysis at large current density

Yong Zhang,[‡a] Liling Liao,[‡a] Haiqing Zhou,[*a] Ying Qi,[a] Jingying Sun,[d] Yan Zhang,[*b] Qian Zhou,[a] Yu Wang,[c] Dongsheng Tang,[a] Fang Yu[*a]

[a]Key Laboratory of Low-Dimensional Quantum Structures and Quantum Control of Ministry of Education, Institute of Interdisciplinary Studies, Key Laboratory for Multifunctional Ionic Electronic Materials and Devices of Hunan Normal University, Changsha 410081, China

[b]Anhui Provincial Key Laboratory of Advanced Catalysis and Energy Materials, School of Chemistry and Chemical Engineering, Anqing Normal University, Anqing 246011, P. R. China

[c]Department of Physics and Texas Center for Superconductivity at the University of Houston (TcSUH), University of Houston, Houston, TX 77204, USA

[d]Instrumental Analysis and Research Center, Sun Yat-sen University, Guangzhou 510275, China

[‡]These authors contributed equally to this work.

Correspondence and requests for materials should be addressed to H.Z. (hqzhou@hunnu.edu.cn), Y.Z. (zyan@hainanu.edu.cn) or F.Y. (fyu@hunnu.edu.cn).

Experimental Section

Chemicals. Nickel(II) nitrate hexahydrate ($Ni(NO_3)_2$ $6H_2O$, Alfa Aesar, 98%), ammonium molybdate (para) tetrahydrate ($(NH_4)_2MoO_4$ $4H_2O$, Alfa Aesar, 98%), cobalt(II) chloride hexahydrate ($CoCl_2$ $6H_2O$, Alfa Aesar, 98%), nickel(II) chloride hexahydrate ($NiCl_2$ $6H_2O$, thermo scientific, 97%), thiourea (CH_4N_2S, Alfa Aesar, 99%), iron (III) nitrate nonahydrate ($Fe(NO_3)_3$ $9H_2O$, Alfa Aesar, ACS 98.0-101.0%), glycerol ($C_3H_8O_3$, BKMAM, 99.0%, AR), DL-glyceric acid ($C_3H_6O_4$, aladdin, 20% in water, 2 mol L^{-1}), glycolic acid ($C_2H_4O_3$, Sigma-Aldrich, 99%), oxalic acid ($C_2H_2O_4$, aladdin, 99.99%), formate ($C_2H_2O_2$, aladdin, 98%), potassium hydroxide (KOH, Alfa Aesar, 45% w/v), deionized water (resistivity: ≥18.2 MΩ·cm at 25 °C) were used for the preparation of all aqueous solutions. All the chemicals were used without further purification.

Synthesis of Ni_3S_2/Co_9S_8 catalyst. The Ni_3S_2/Co_9S_8 nanosheet catalyst was vertically grown on porous nickel foam via a hydrothermal method. Initially, 0.3 mmol of $CoCl_2$ $6H_2O$ and 2 mmol of CH_4N_2S were dissolved in 20 mL of deionized water, and stirred vigorously for 15 minutes until fully dissolved. Subsequently, the solution was transferred to a Teflon autoclave along with Ni foam (2×4 cm^2) that had been cleaned with 3 M HCl, alcohol and deionized water via ultrasonication for 10 minutes. The reaction was conducted under heating at 120 °C for 12 h in a drying oven. The resultant samples were washed with deionized water and dried at room temperature to obtain the Ni_3S_2/Co_9S_8 nanosheet catalyst.

Synthesis of Fe-Ni_3S_2/Co_9S_8 catalyst. 0.25-0.75 g $Fe(NO_3)_3$ $9H_2O$ was dissolved thoroughly in 5 mL alcohol solution as the iron precursor. Then the as-obtained Ni_3S_2/Co_9S_8 nanosheet samples were immersed in the iron solution for a few seconds, which were dried in air for approximately 17 h. Finally, the iron-modified Ni_3S_2/Co_9S_8 nanosheet catalyst

($Fe-Ni_3S_2/Co_9S_8$) was obtained.

Synthesis of Ni_3S_2/Co_9S_8/FeNiN catalyst. The $Fe-Ni_3S_2/Co_9S_8$ sample was transferred to the central zone of a tube furnace, using high-purity ammonia gas and inert argon gas as nitrogen source and protective gas, respectively. The temperature was ramped up to 350 ℃ at a rate of 5 ℃ min^{-1} and maintained at this temperature for 2 h for thermal nitridation treatment. After the nitridation process, the tube furnace were cooled down to room temperature to prepare the Ni_3S_2/Co_9S_8/FeNiN catalyst.

Synthesis of NiMoN catalyst. Initially, $NiMoO_4$ nanorods were synthesized in situ on Ni foam via a hydrothermal method. 0.04 M $Ni(NO_3)_2 \cdot 6H_2O$ and 0.04 M $(NH_4)_2MoO_4 \cdot 4H_2O$ were dissolved in 40 mL deionized water. Subsequently, the fully dissolved solution and Ni foam, which had been cleaned with 3 M HCl, were transferred together into a Teflon autoclave. The mixture was then incubated at 150 ℃ for 6 h. After the hydrothermal reactor cooled down to room temperature, the resultant materials were removed and dried to obtain $NiMoO_4$ nanorods. These nanorod samples were then placed in a tube furnace, where ammonia gas was used as the nitrogen source. The temperature was increased to 400 ℃ at a rate of 5 ℃ min^{-1} and maintained for 3 h. Upon cooling down, the NiMoN catalyst was successfully prepared.

Synthesis of NiS or CoS catalysts. Initially, 0.3 mmol of $NiCl_2 \cdot 6H_2O$ or $CoCl_2 \cdot 6H_2O$ and 2 mmol of CH_4N_2S were dissolved in 20 mL deionized water under continuous magnetic stirring for 15 min to ensure complete dissolution. A piece of Ni or Co foam (2×4 cm^2), pretreated by ultrasonic cleaning in 3 M HCl, anhydrous ethanol and deionized water for 10 min each, was then added to the solution. The mixture was transferred into a Teflon autoclave and maintained at 120 °C in a drying oven for 12 h. After naturally cooling down to room temperature, the resultant catalyst was thoroughly rinsed with deionized water and dried under ambient conditions.

Synthesis of FeN-NiS or FeN-CoS catalysts. Firstly, 0.25-0.75 g of $Fe(NO_3)_3$ $9H_2O$ was dissolved in 5 mL of ethanol to prepare the precursor solution. The air-dried NiS or CoS catalyst was then briefly immersed in the iron precursor solution for a few seconds, removed, and allowed to dry naturally in a fume hood for approximately 17 h. Subsequently, the Fe-modified NiS or CoS catalyst was placed in the central zone of a tubular furnace and subjected to thermal nitridation under a mixed atmosphere of high-purity ammonia (as the nitrogen source) and argon (as the protective gas). The temperature was ramped to 350 °C at a rate of 5 °C min^{-1} and held for 2 h. After cooling down to room temperature, the FeN-NiS or FeN-CoS catalyst was obtained.

Material characterization. The morphology of the samples was characterized by scanning electron microscope (SEM, MIRA4 LMH, TESCAN). X-ray diffraction (XRD) was employed for crystal structure characterization of the catalysts (XRD, D8 Discover, Bruker). X-ray photoelectron spectroscopy (XPS, ESCALAB250Xi, Thermo Fisher Scientific) was employed to investigate the surface composition and chemical states of the catalysts. The analysis involved quasi in-situ X-ray photoelectron spectroscopy (XPS) using an XPS system connected to a customized vacuum glove box (Suzhou Vigor Technologies Co., Ltd.) and transfer chamber system. High-resolution transmission electron microscopy (HRTEM, TecnaiG2 F20, FEI) equipped with an energy-dispersive X-ray spectrometer (EDS). The potential-dependent Raman spectroscopy measurements of GOR and OER were conducted using a microscope system (LabRAM HR, Horiba) equipped with a semiconductor laser (λ=532 nm). The analysis of glycerol oxidation product concentration changes primarily utilized a high-performance liquid chromatography (HPLC, LC-20A, SHIMADZU) equipped with a refractive index detector (RID-20A) and an organic acid column (Aminex HP-87H Column 300 × 7.8 mm). In-situ electrochemical impedance spectroscopy (EIS) testing was conducted using an electrochemical workstation at different potentials (1.1 V-1.7 V) over a frequency range of 100000 to 0.1 Hz.

Electrochemical measurements. All the electrochemical tests for OER and GOR were carried out at room temperature using the electrochemical workstations (Gamry Reference 5000 or 1010E), which feature a typical three-electrode configuration. The electrocatalysts prepared on Ni foam were directly employed as the working electrode, while a graphite paper and Hg/HgO were used as the counter and reference electrodes, respectively. The OER testing was conducted in 1 M KOH, while the GOR testing was performed in 1 M KOH with 0.1 M glycerol. According to the following equation, all the potentials were calibrated to the reversible hydrogen electrode (RHE) potential: $E(\text{vs RHE}) = E(\text{vs Hg/HgO}) + 0.05916 \times \text{pH} + 0.098$. The linear sweep voltammetry and cyclic voltammetry curves were obtained at scan rates of 2 mV s^{-1} and 1 mV s^{-1}, respectively. During the OER or GOR process, electrochemical impedance spectroscopy (EIS) was measured at 1.53 V (vs. RHE) with the frequencies ranging from 100 kHz to 0.1 Hz. The Tafel slopes were obtained through logarithmic transformation of the linear polarization curves, conforming to the Tafel equation [$\eta = \text{b}\log j + \text{a}$], where η, j and b represent overpotential, current density and Tafel slope, respectively. Cyclic voltammetry curves recorded at different scan rates (10-100 mV s^{-1}) were utilized to measure the electrochemical double-layer capacitance (C_{dl}) of the electrode in the non-Faradaic region, aiming to assess the electrochemical active surface areas (ECSAs) of the electrode. Chronopotentiometry was employed to assess the stability of the catalysts for OER, GOR or two-electrode electrolyzers. Unless otherwise specified, iR compensation was conducted for all the polarization curves.

Product analysis. The glycerol oxidation products were qualitatively and quantitatively analyzed by high-performance liquid chromatography (HPLC). For each analysis, 150 μL of the electrolyte was diluted to 1.5 mL with 0.5 M H_2SO_4, and then transferred to the sample bottle.

The HPLC injection volume was 10 μL, and separation was performed using an Aminex HP-87H column (300 × 7.8 mm). The mobile phase consisted of 5 mM H_2SO_4, and the column temperature was maintained at 40 ℃, with a constant flow rate of 0.6 mL min^{-1} and elution for 20 min. The composition of electrolyte products was determined by the retention time of elution peaks, and product concentrations were determined according to the established standard curves of standard substances. Further calculations were conducted to determine the glycerol conversion (η_{GLY}), faradaic efficiency (FE), yield (Y), and selectivity (S) of the relevant products.

The glycerol conversion (η_{GLY}) can be determined by the following equations:

$$\eta_{GLY} = \frac{C_{0,GLY} - C_{GLY}}{C_{0,GLY}} \times 100\%$$

where $C_{0,GLY}$ and C_{GLY} represent the initial and final concentration of glycerol.

The selectivity (S) and yield (Y) of the relevant products can be determined by the following equations:

$$S_{product} = \frac{C_{product} \times \alpha}{C_{0,GLY} - C_{GLY}} \times 100\%$$

$$Y_{products} = \frac{C_{product} \times \alpha}{C_{0,GLY}} \times 100\%$$

where $C_{0,GLY}$ represents the initial concentration of glycerol, C_{GLY} represents the final concentration of glycerol, $C_{product}$ represents the concentrations of the relevant electrolytic products, and the factor α is associated with C_3 (α=1), C_2 (α=2/3) or C_1 (α=1/3) products, as for every equivalent of C_3, C_2, or C_1 product produced, 1, 2/3, or 1/3 equivalents of glycerol are consumed.

The FE (%) of products formation can be determined by the following equations:

$$FE_{product} = \frac{z \times C_{product} \times V \times F}{Q_{total}} \times 100\%$$

where Q_{total} represents the total charge passed during the reaction period, F is the Faraday constant (96485 C mol^{-1}), $C_{product}$ represents the concentrations of the relevant electrolytic products, V is the volume of the electrolyte, and z is the number of electrons transferred per mole of product generated.

Balanced half-reactions for each potential product during glycerol oxidation, along with the determination of z (the number of electrons) involved:

GLY → GLAD: $C_3H_8O_3 + 2OH^{-} \rightarrow C_3H_6O_3 + 2H_2O + 2e^{-}$ z=2

GLY → GLA: $C_3H_8O_3 + 5OH^{-} \rightarrow C_3H_5O_4^{-} + 4H_2O + 4e^{-}$ z=4

GLY → GCA: $C_3H_8O_3 + 13/2OH^{-} \rightarrow 3/2C_2H_3O_3^{-} + 5H_2O + 5e^{-}$ z=10/3

GLY → TA: $C_3H_8O_3 + 10OH^{-} \rightarrow C_3H_2O_5^{2-} + 8H_2O + 8e^{-}$ z=8

GLY → OA: $C_3H_8O_3 + 14OH^{-} \rightarrow 3/2C_2O_4^{2-} + 11H_2O + 11e^{-}$ z=22/3

GLY → FA: $C_3H_8O_3 + 11OH^{-} \rightarrow 3HCOO^{-} + 8H_2O + 8e^{-}$ z=8/3

GLY → DHA: $C_3H_8O_3 + 2OH^{-} \rightarrow C_3H_6O_3 + 2H_2O + 2e^{-}$ z=2

GLY → GCAD: $2C_3H_8O_3 + 4OH^{-} \rightarrow 3C_2H_4O_2 + 4H_2O + 4e^{-}$ z=4/3

where GLY, GLAD, GLA, GCA, TA, OA, FA, DHA and GCAD represents glycerol, glyceraldehyde, glycerate, glycolate, tartronate, oxalate, formate, dihydroxyacetone and glycolaldehyde, respectively.

Computational methods. Our simulations were performed within the framework of density functional theory (DFT) implemented in the Quantum Espresso package (QE).[1,2] The exchange-correlation energies were described using the generalized gradient approximation (GGA) with the Perdew-Burke-Ernzerhof (PBE) functional.[3,4] The projected augmented wave (PAW) method[5] was employed for the pseudo-potentials of the C, H, O, N, S, Ni, Fe and Co-atoms, and the convergence criteria for the maximum force and energy on each atom during structure relaxation were set to 0.02 eV $Å^{-1}$and 10^{-5} eV. The Brillouin-zone sampling was conducted using Monkhorst-Pack (MP) grids of special points with the separation of 0.04 $Å^{-1}$.

For the structural optimization and the electronic structure calculations, respectively. The lattice parameters and atomic positions were relaxed with a convergence criterion for the total energy and the ionic forces set to 10^{-5} eV and 0.02 eV $Å^{-1}$, respectively. A semiempirical DFT-D3 force-field approach was used to include the physical van der Waals (vdW) interaction in our calculations.[6,7]

The adsorption energy (E_b) was defined according to the equation:

$$E_b = E_{t1} - E_{s1} - E_{s2}$$

where E_{t1} is the total energy of the binding system, E_{s1} is the energy of the optimized clean bluks, and E_{s2} is the energy of the adsorbates in vacuum.

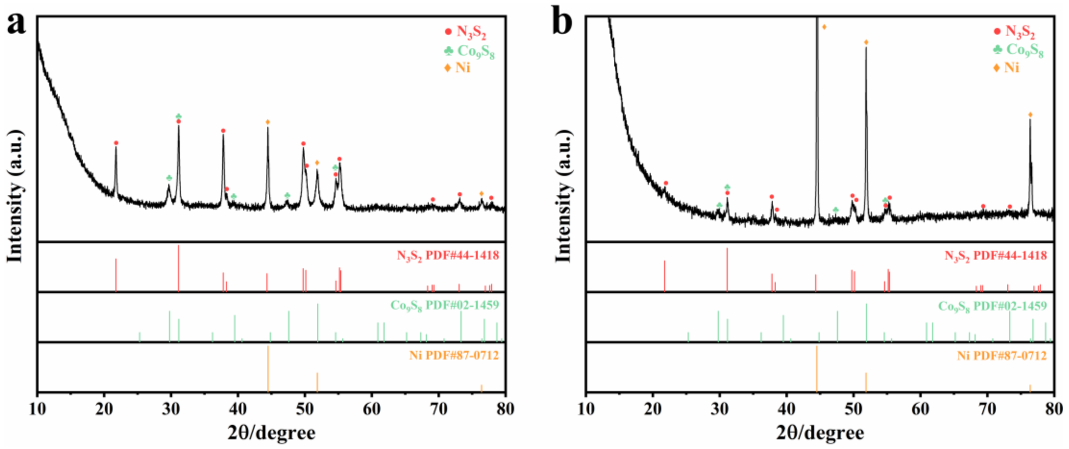

Figure S1. Typical XRD patterns of (a) Ni_3S_2/Co_9S_8 and (b) Fe-Ni_3S_2/Co_9S_8.

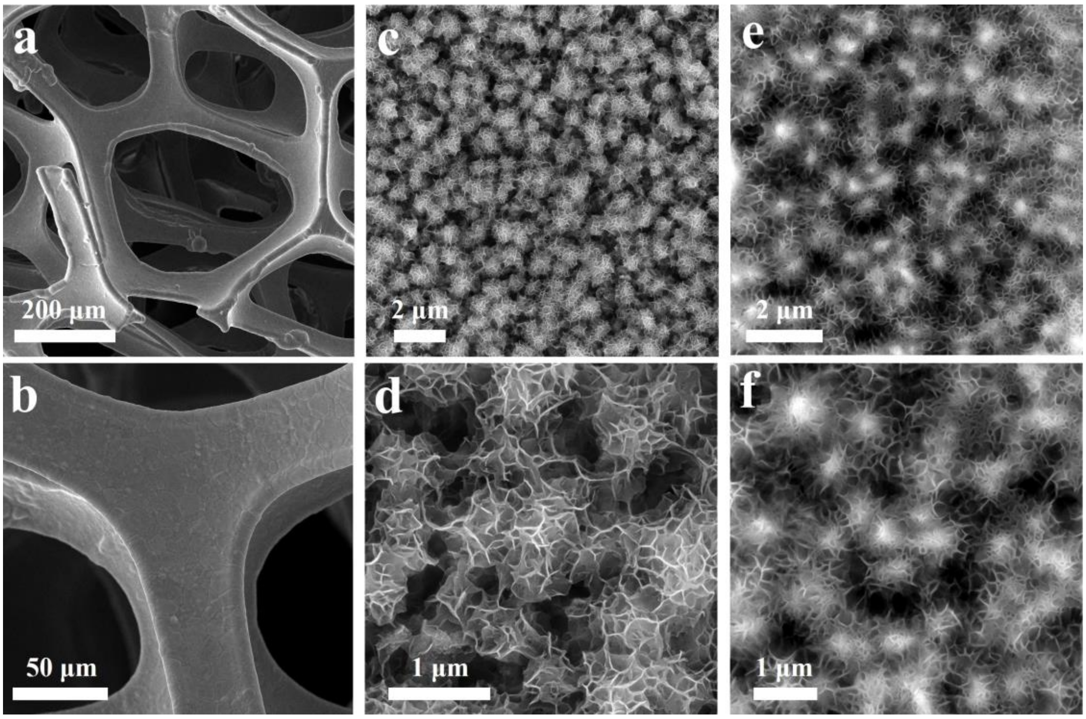

Figure S2. (a,b) Typical SEM images of bare Ni foam. (c,d) SEM images of Ni_3S_2/Co_9S_8. (e,f) SEM images of Fe-Ni_3S_2/Co_9S_8.

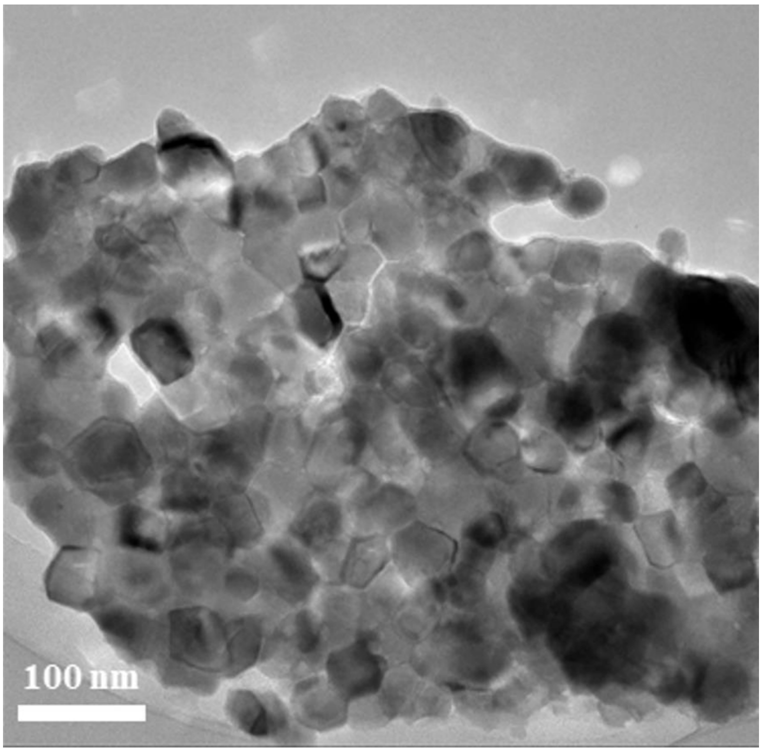

Figure S3. A typical TEM image of Ni_3S_2/Co_9S_8/FeNiN catalyst.

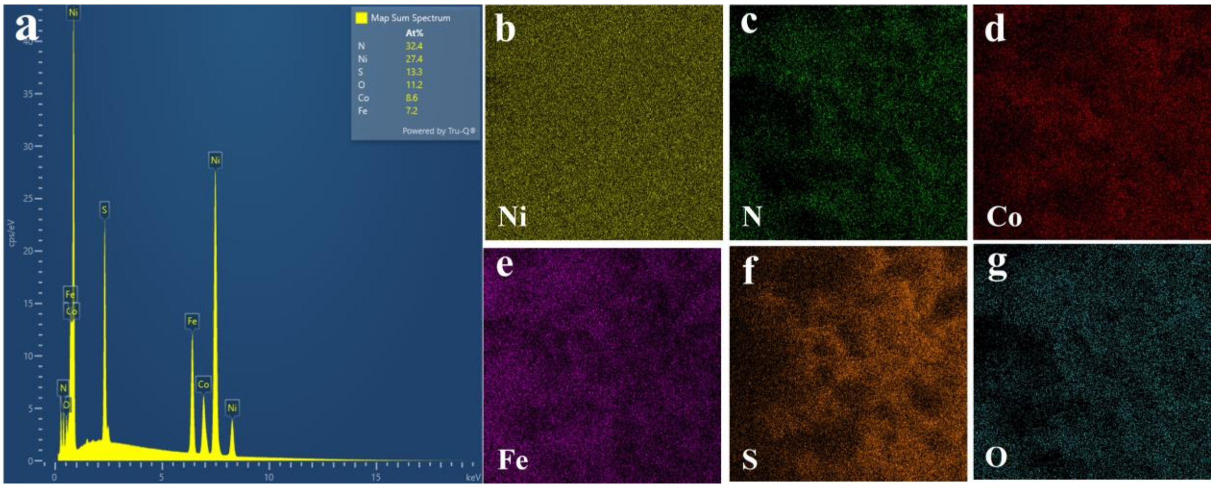

Figure S4. (a) Energy-dispersive X-ray spectrum. (b-g) Elemental mapping images of the $Ni_3S_2/Co_9S_8/FeNiN$ catalyst.

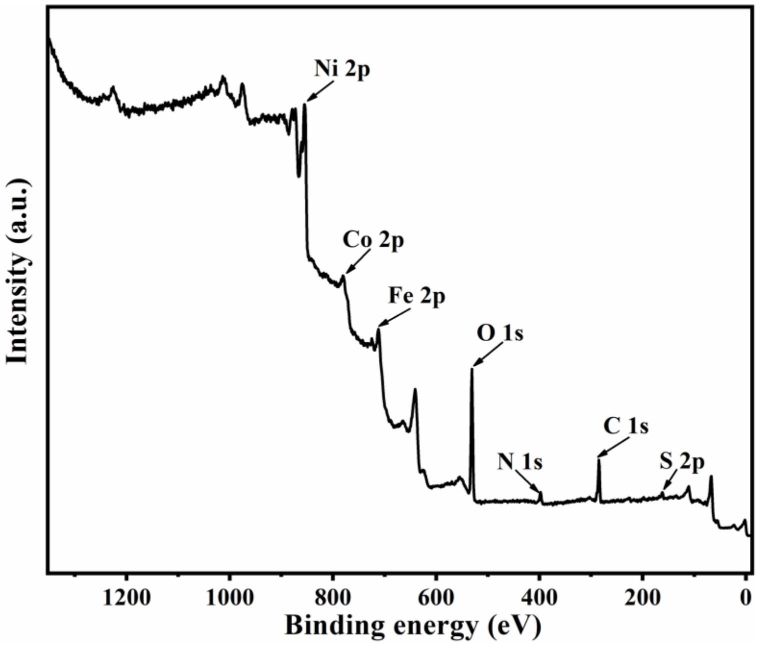

Figure S5. The XPS survey spectrum of $Ni_3S_2/Co_9S_8/FeNiN$ catalyst.

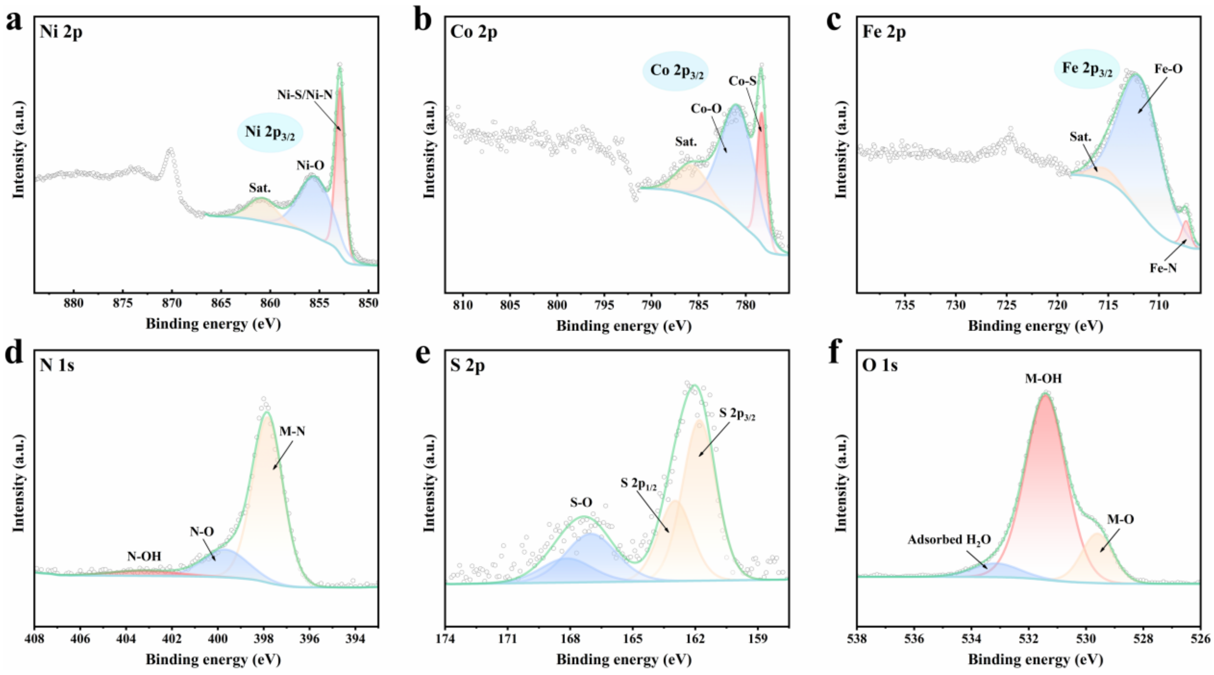

Figure S6. The elaborate XPS analysis of the as-prepared Ni_3S_2/Co_9S_8/FeNiN samples: (a) Ni 2p, (b) Co 2p, (c) Fe 2p, (d) S 2p, (e) N 1s and (f) O 1s.

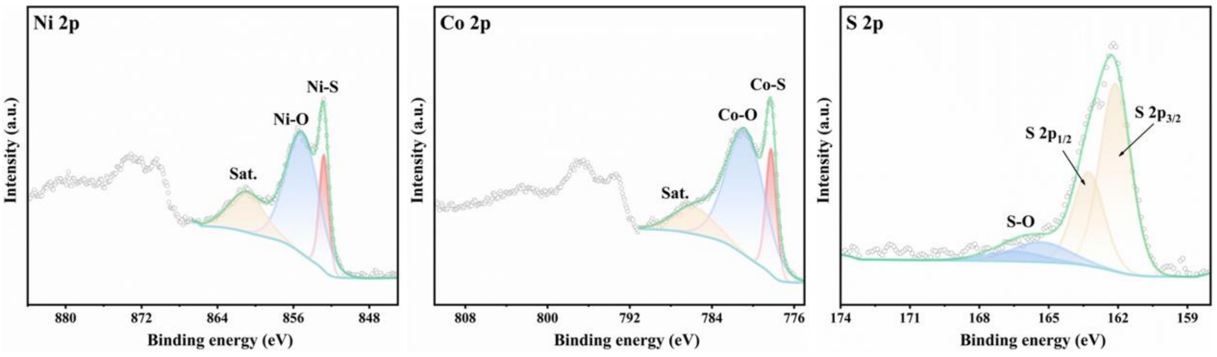

Figure S7. Ni 2p, Co 2p and S 2p XPS spectra of the as-prepared Ni_3S_2/Co_9S_8 samples.

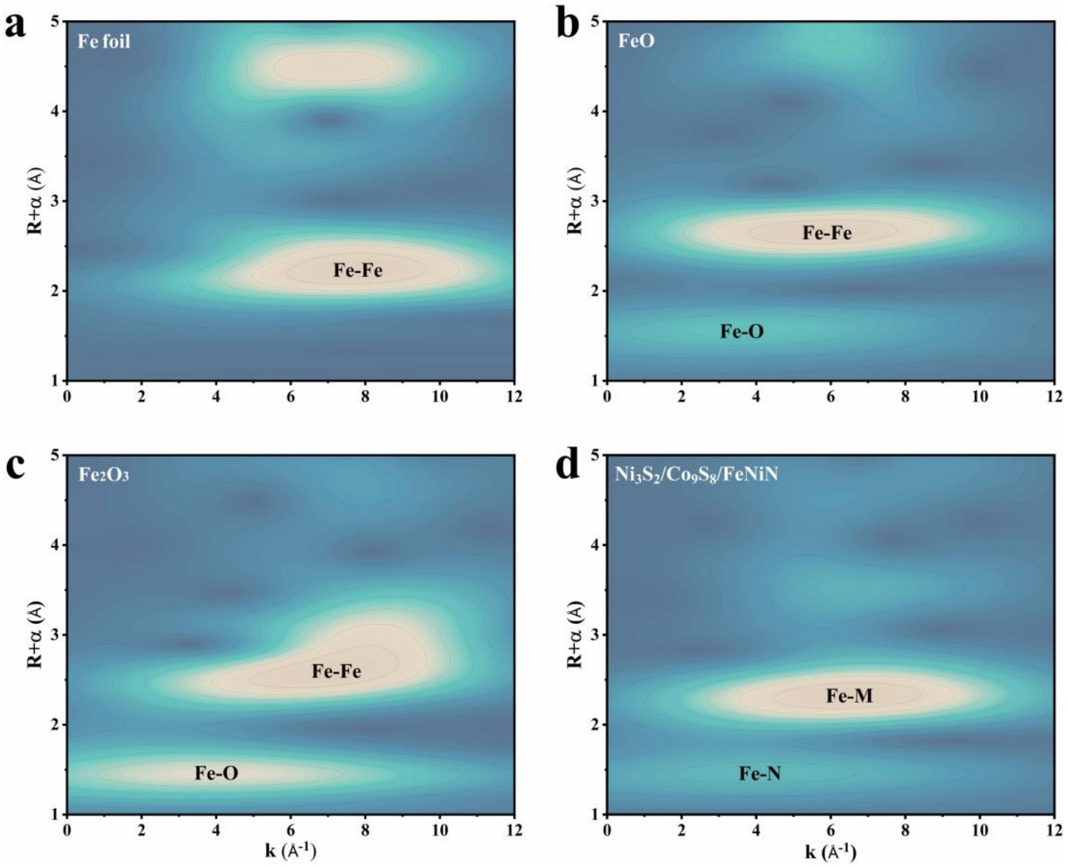

Figure S8. Wavelet transform for the k^3-weighted EXAFS signals of (a) Fe foil, (b) FeO, (c) Fe_2O_3 and (d) Ni_3S_2/Co_9S_8/FeNiN catalyst.

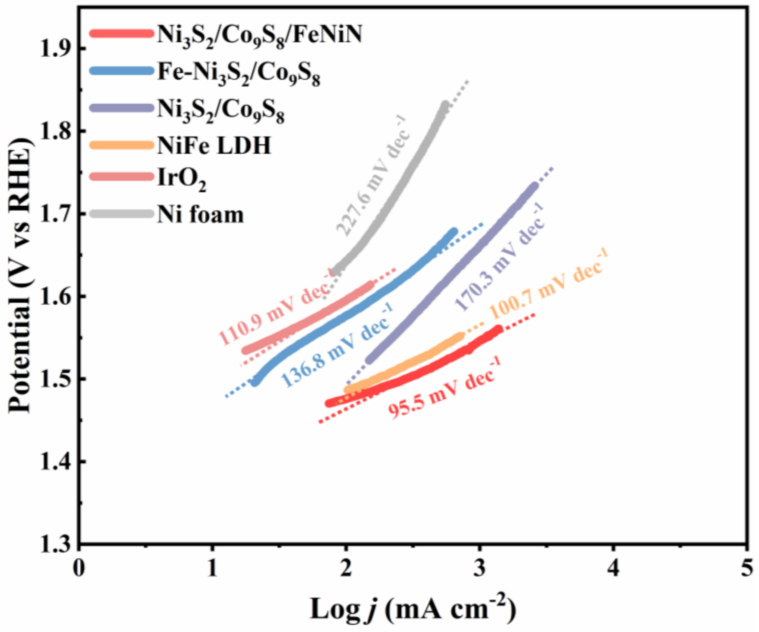

Figure S9. Tafel analysis of different OER electrocatalysts in 1 M KOH.

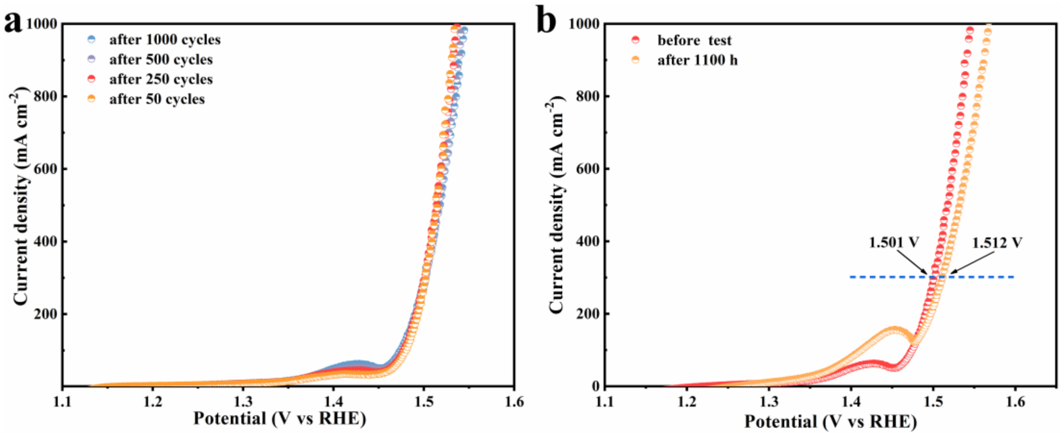

Figure S10. (a) Cyclic stability tests of Ni_3S_2/Co_9S_8/FeNiN for OER. (b) The OER polarization curves of Ni_3S_2/Co_9S_8/FeNiN before and after continuous operation for 1100 hours.

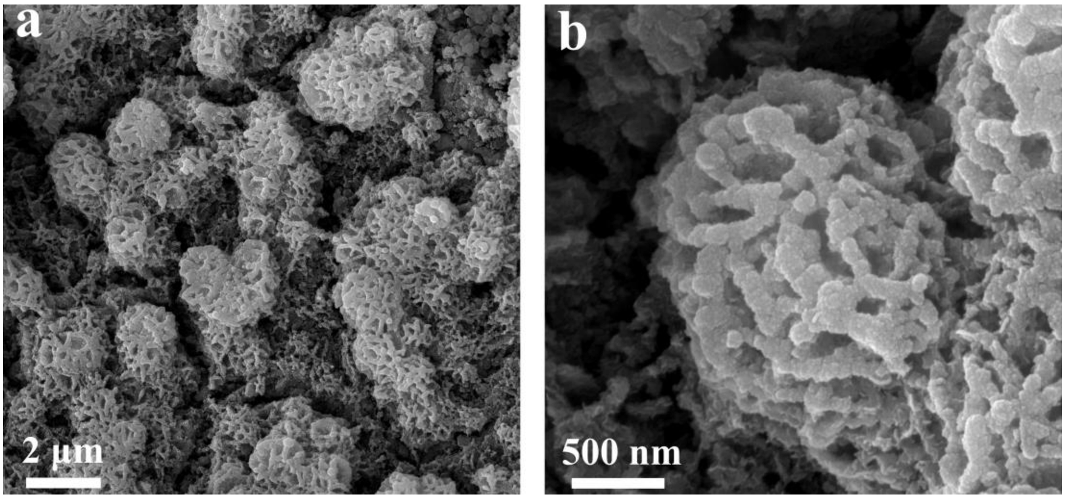

Figure S11. Typical SEM images of Ni_3S_2/Co_9S_8/FeNiN after OER testing.

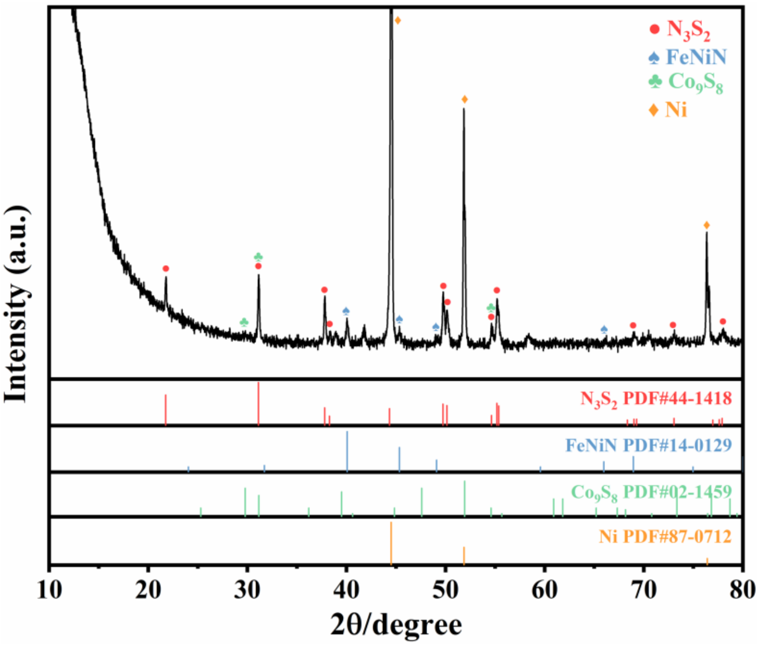

Figure S12. A typical XRD pattern of post-OER Ni_3S_2/Co_9S_8/FeNiN catalyst.

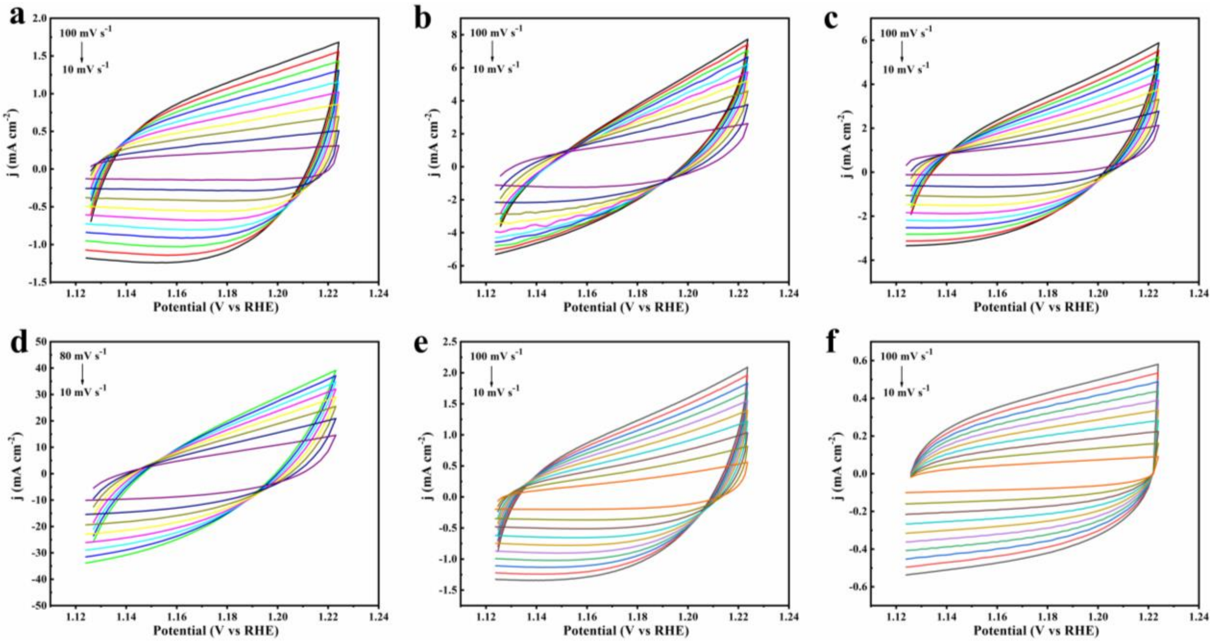

Figure S13. Cyclic voltammetry curves of (a) Ni foam, (b) Ni_3S_2/Co_9S_8, (c) Fe-Ni_3S_2/Co_9S_8, (d) Ni_3S_2/Co_9S_8/FeNiN, (e) NiFe LDH and (f) IrO_2 for OER with scan rates from 10 to 100 mV s^{-1}.

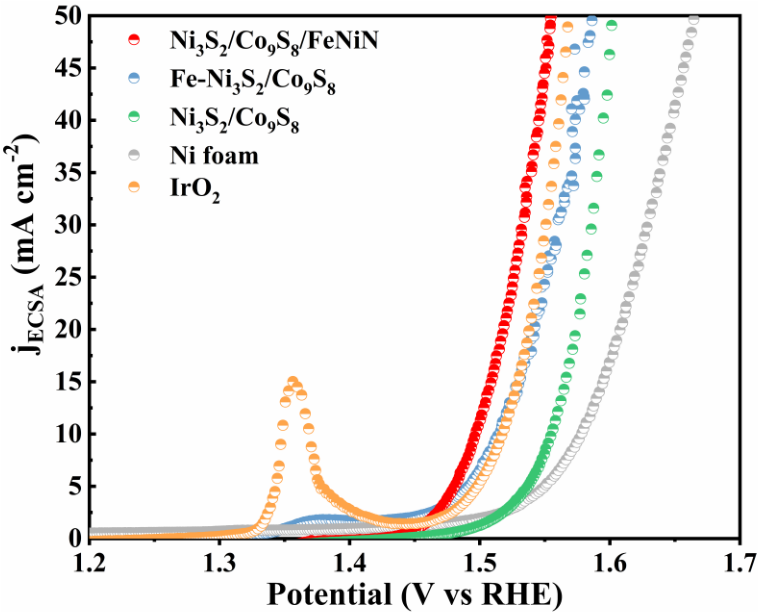

Figure S14. C_{dl}-normalized polarization curves of different catalysts for OER.

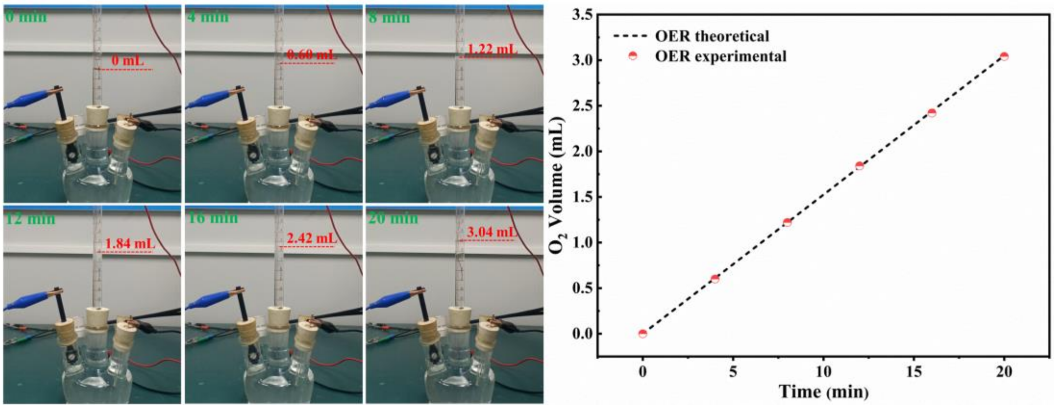

Figure S15. Measuring O_2 gas volume using a drainage method during the OER catalysis at 200 mA cm^{-2} (40 mA) in 1 M KOH.

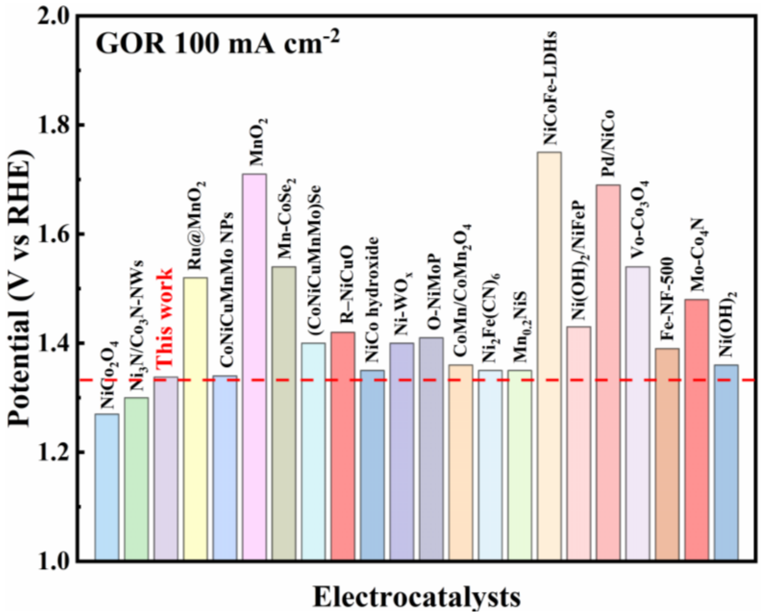

Figure S16. Comparison of GOR potentials at 100 mA cm^{-2} for recently reported transition metal-based electrocatalysts for organic molecule electrooxidation.

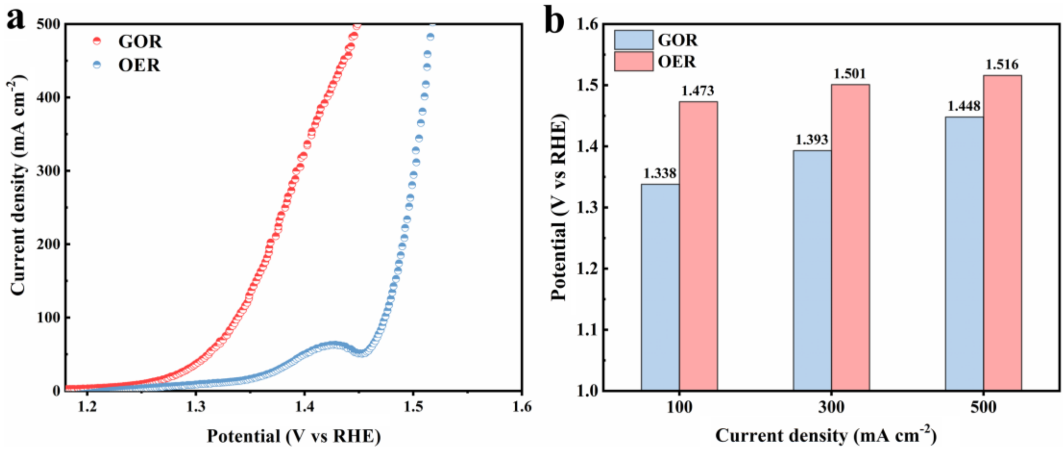

Figure S17. (a) The GOR and OER polarization curves of Ni_3S_2/Co_9S_8/FeNiN catalyst. (b) The corresponding potential histograms at different current densities of 100, 300, and 500 mA cm^{-2} for GOR and OER.

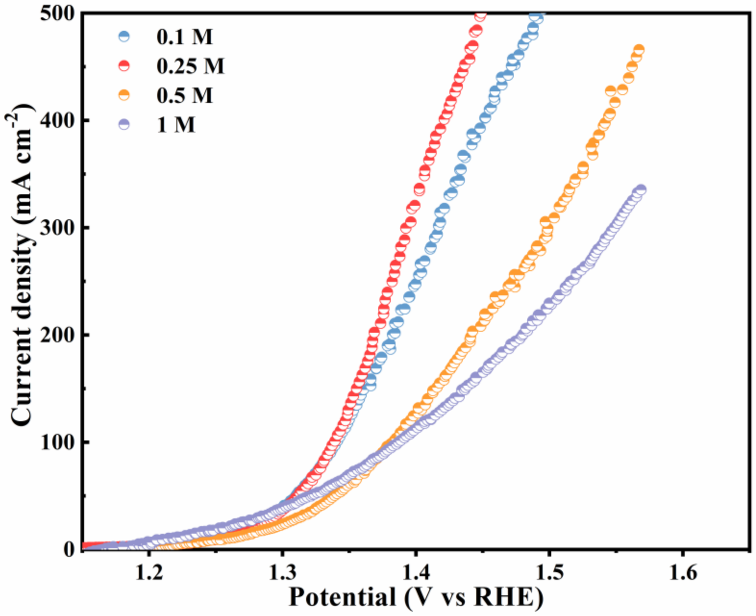

Figure S18. The GOR polarization curves of $Ni_3S_2/Co_9S_8/FeNiN$ catalyst modified with different iron nitrate concentrations.

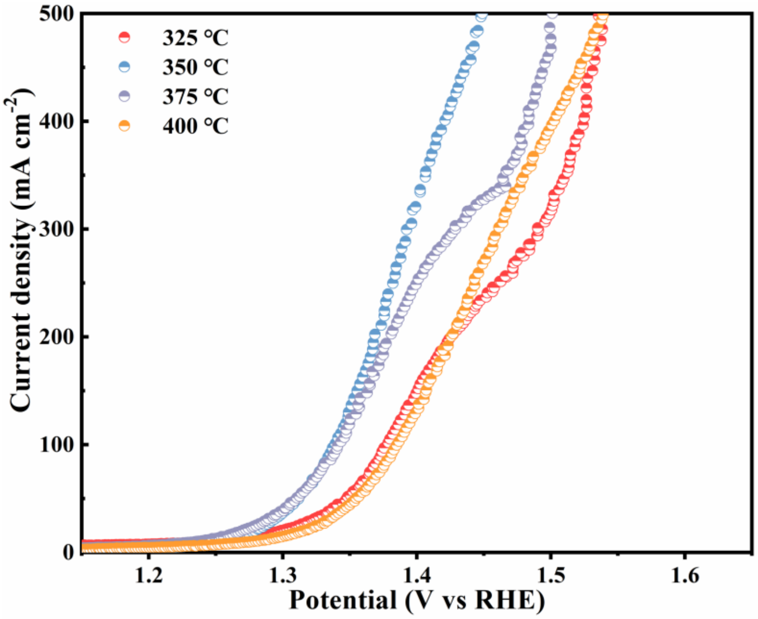

Figure S19. The GOR polarization curves of $Ni_3S_2/Co_9S_8/FeNiN$ catalyst synthesized at different nitridation temperature.

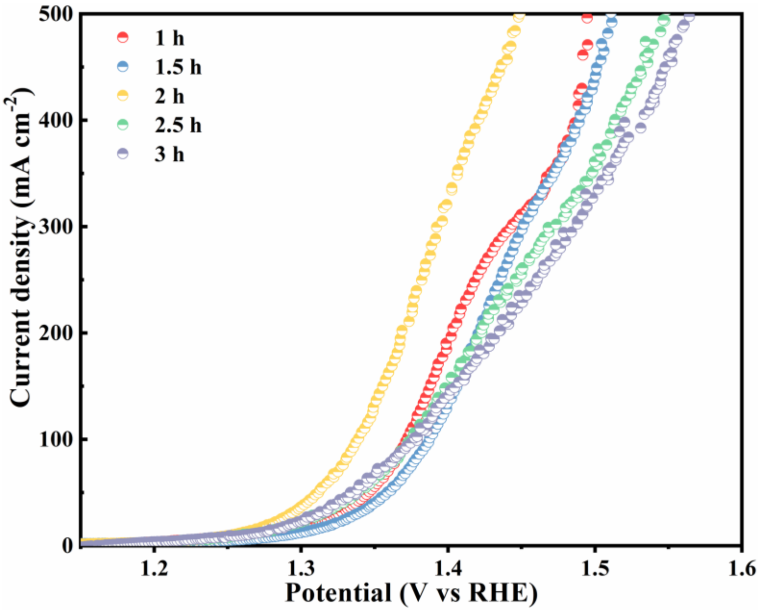

Figure S20. The GOR polarization curves of Ni_3S_2/Co_9S_8/FeNiN catalyst under different nitridation duration.

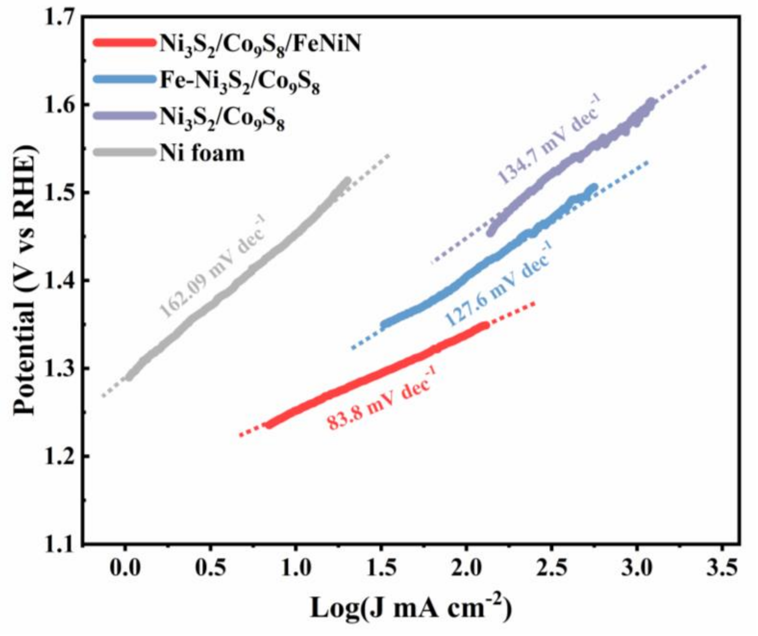

Figure S21. Tafel slopes of different catalysts for GOR in 1 M KOH with 0.1 M glycerol.

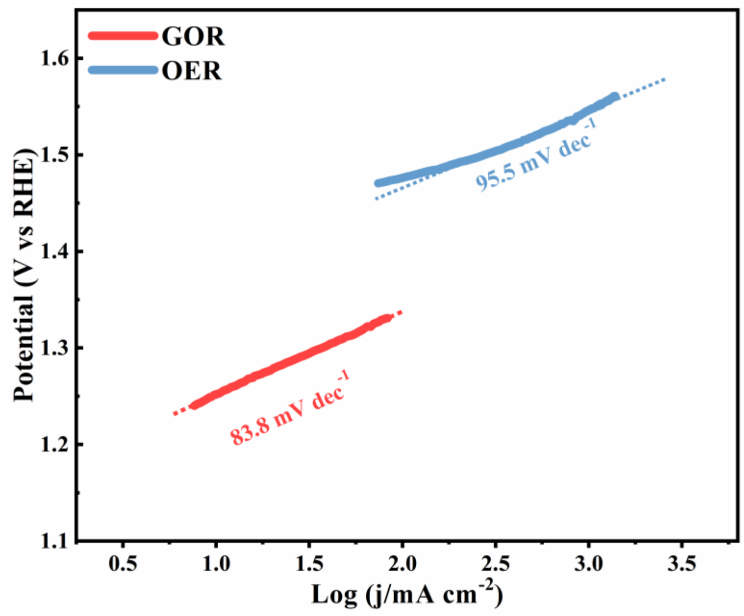

Figure S22. Comparison of Tafel slopes for GOR and OER.

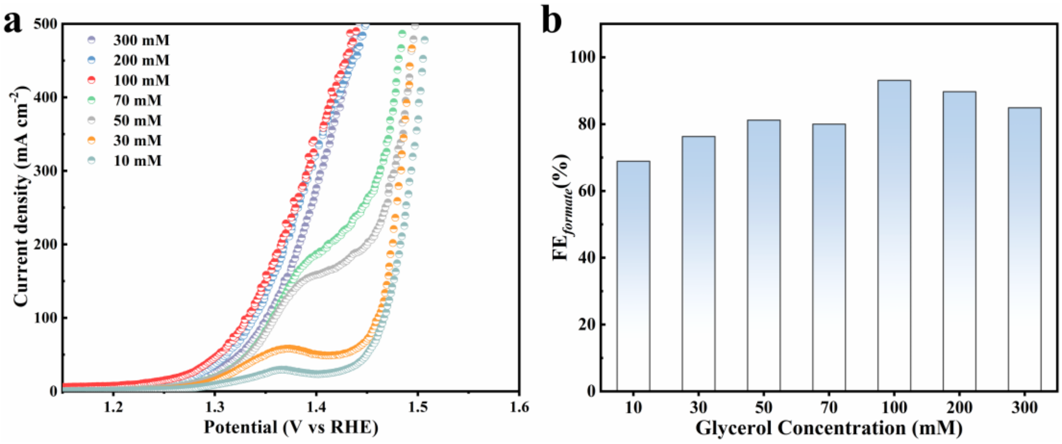

Figure S23. (a) The GOR polarization curves in 1 M KOH electrolyte with different glycerol concentrations. (b) The corresponding FEs of formate production detected with a total charge of 40 C passed at 1.35 V.

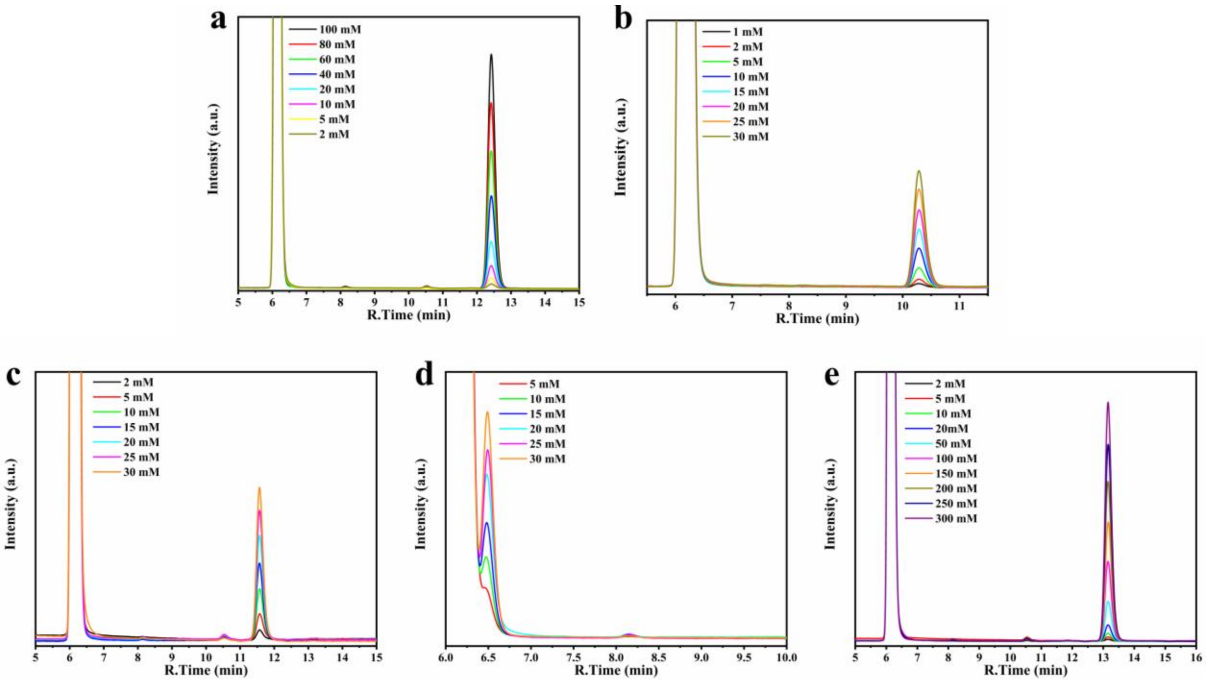

Figure S24. HPLC chromatograms of (a) glycerol, (b) glycerate, (c) glycolate, (d) oxalate and (e) formate.

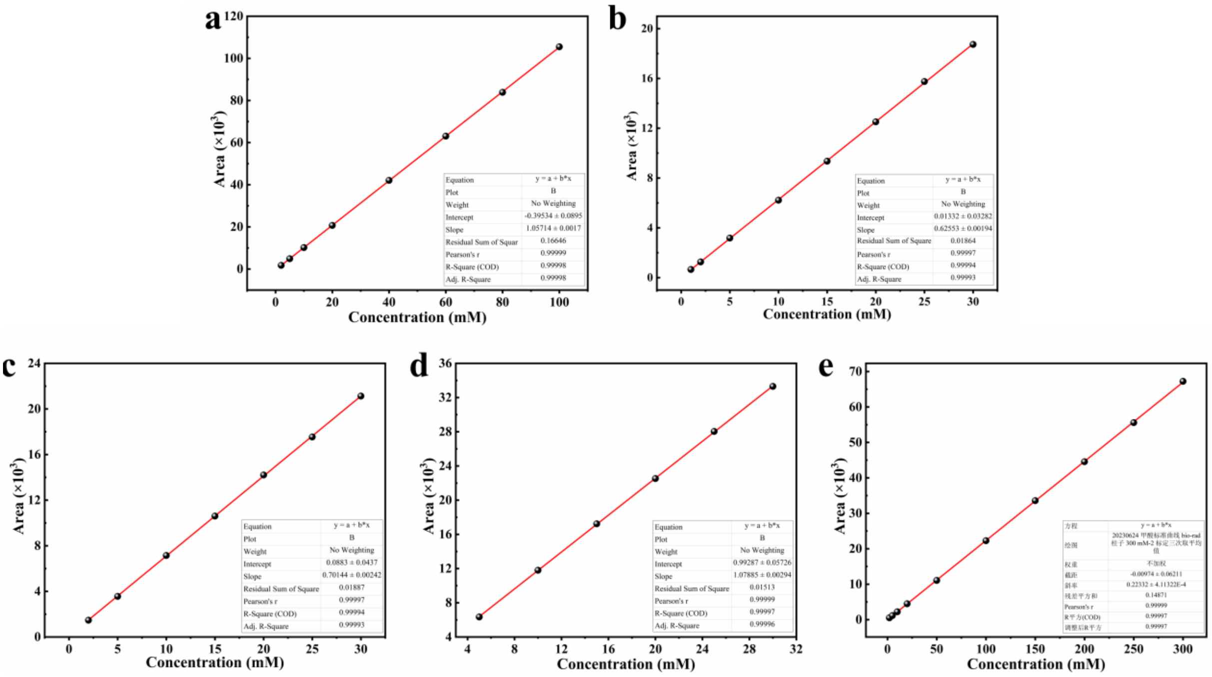

Equation	y = a + b*x
Plot	B
Weight	No Weighting
Intercept	-0.39534 ± 0.0895
Slope	1.05714 ± 0.0017
Residual Sum of Squar	0.16646
Pearson's r	0.99999
R-Square (COD)	0.99998
Adj. R-Square	0.99998

Equation	y = a + b*x
Plot	B
Weight	No Weighting
Intercept	0.01332 ± 0.03282
Slope	0.62553 ± 0.00194
Residual Sum of Square	0.01864
Pearson's r	0.99997
R-Square (COD)	0.99994
Adj. R-Square	0.99993

Equation	y = a + b*x
Plot	B
Weight	No Weighting
Intercept	0.0883 ± 0.0437
Slope	0.70144 ± 0.00242
Residual Sum of Square	0.01887
Pearson's r	0.99997
R-Square (COD)	0.99994
Adj. R-Square	0.99993

Equation	y = a + b*x
Plot	B
Weight	No Weighting
Intercept	0.99287 ± 0.05726
Slope	1.07885 ± 0.00294
Residual Sum of Square	0.01513
Pearson's r	0.99999
R-Square (COD)	0.99997
Adj. R-Square	0.99996

方程	y = a + b*x
绘图	20230624 甲酸标准曲线 bio-rad 柱子 300 mM-2 标定三次取平均值
权重	不加权
截距	-0.00974 ± 0.06211
斜率	0.22332 ± 4.11322E-4
残差平方和	0.14871
Pearson's r	0.99999
R平方(COD)	0.99997
调整后R平方	0.99997

Figure S25. HPLC standard curves of (a) glycerol, (b) glycerate, (c) glycolate, (d) oxalate and (e) formate.

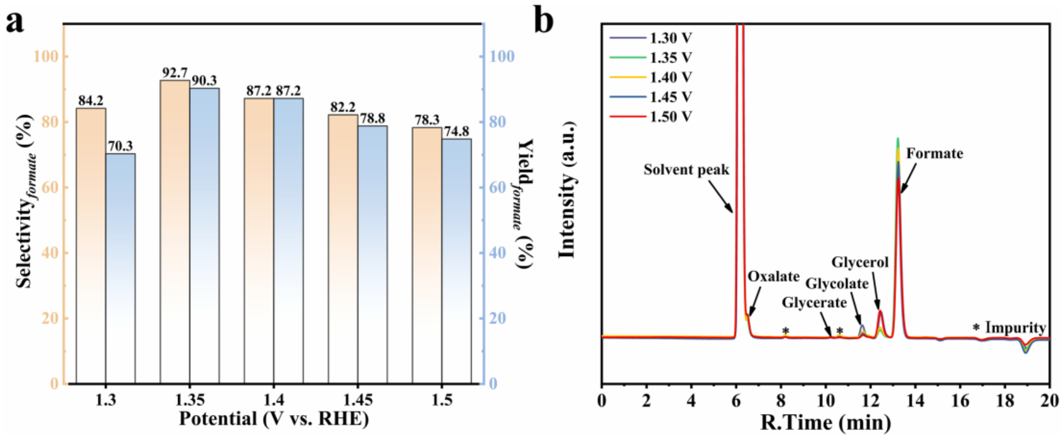

Figure S26. Selectivity and yield of formate after the glycerol oxidation at different applied potentials in 1 M KOH+0.1 M GLY electrolyte with a total charge of 231 C passed.

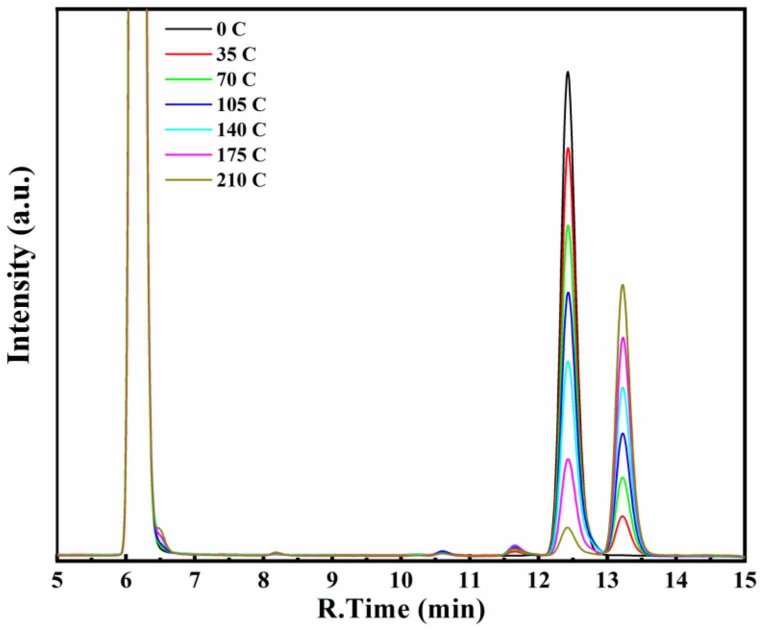

Figure S27. HPLC chromatograms of glycerol oxidation products after passing different Coulombic quantities using Ni_3S_2/Co_9S_8/FeNiN catalyst as the electrocatalyst at 1.35 V (vs RHE) in 1 M KOH with 0.1 M glycerol.

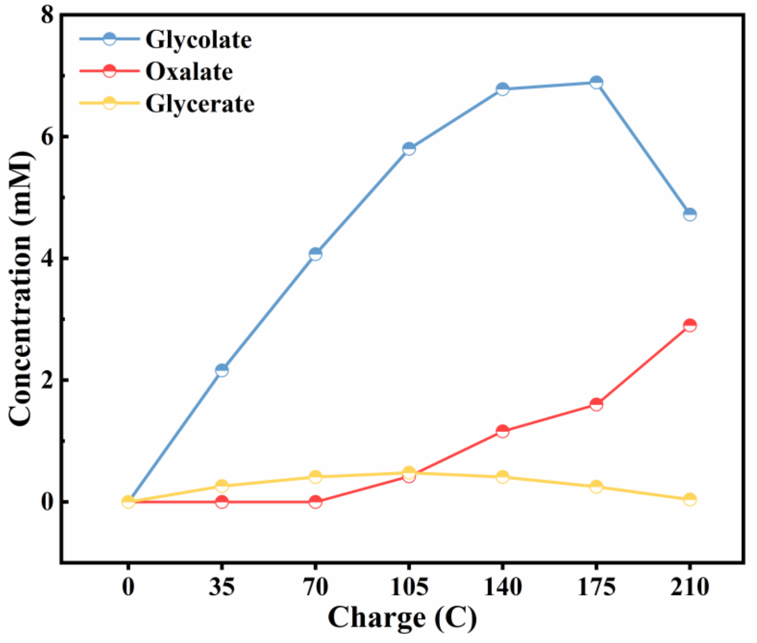

Figure S28. The concentration of the glycerate, glycolate and oxalate varies with coulombic quantity at 1.35 V in a 1 M KOH electrolyte with 0.1 M glycerol.

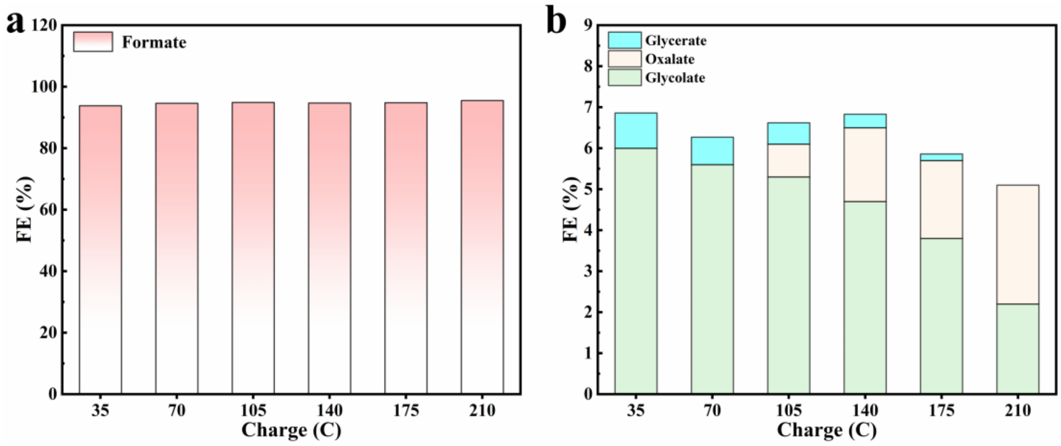

Figure S29. The Faradaic efficiency toward (a) the main value-added product of formate, and (b) other value-added products after glycerol oxidation with different coulombic quantities at 1.35 V in 1 M KOH with 0.1 M glycerol.

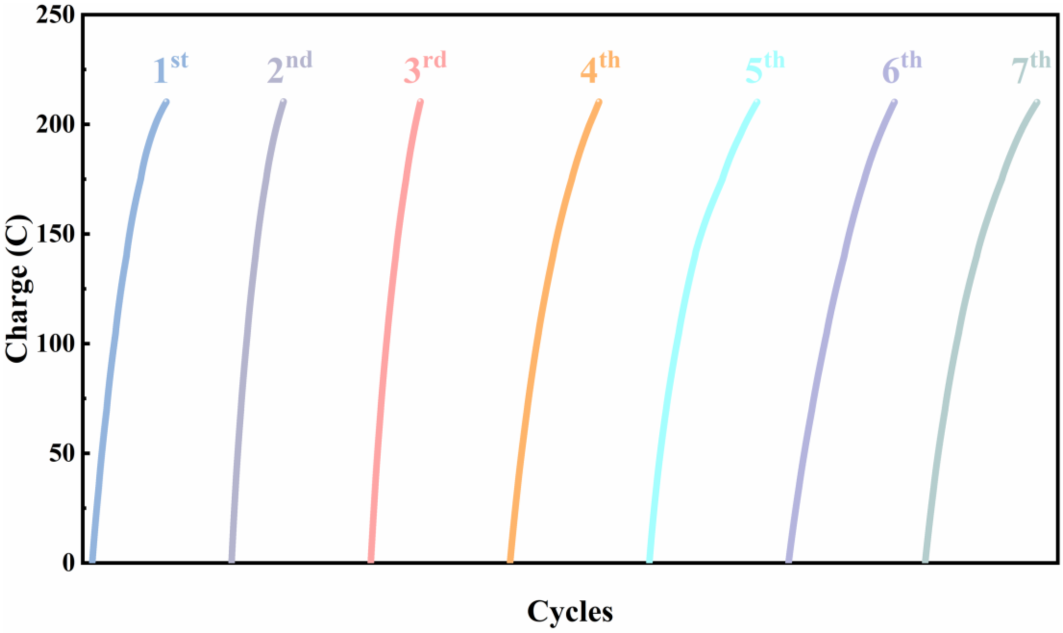

Figure S30. The GOR durability test of Ni_3S_2/Co_9S_8/FeNiN catalyst. The seven successive electrolysis cycles with a total charge of 210 C passed at 1.35 V.

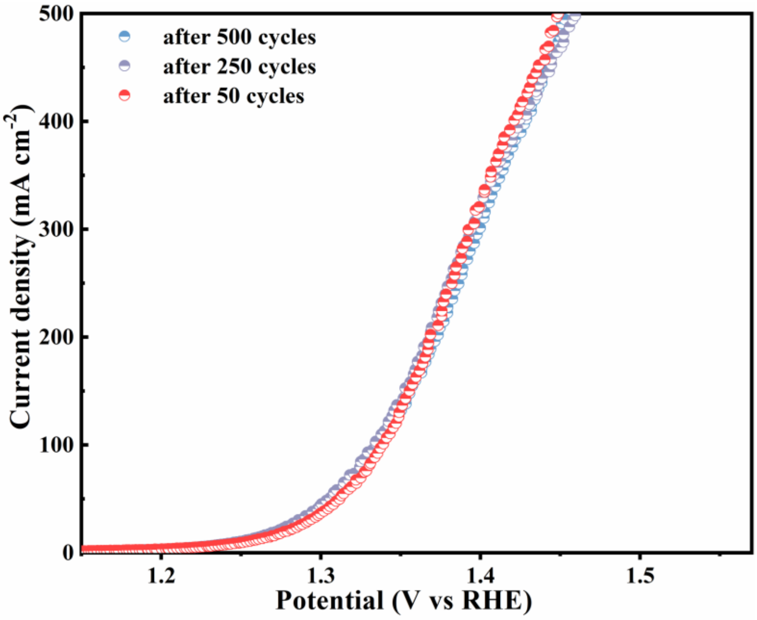

Figure S31. The polarization curves of Ni_3S_2/Co_9S_8/FeNiN catalyst after different cyclic voltammetric tests in 1 M KOH with 0.1 M glycerol.

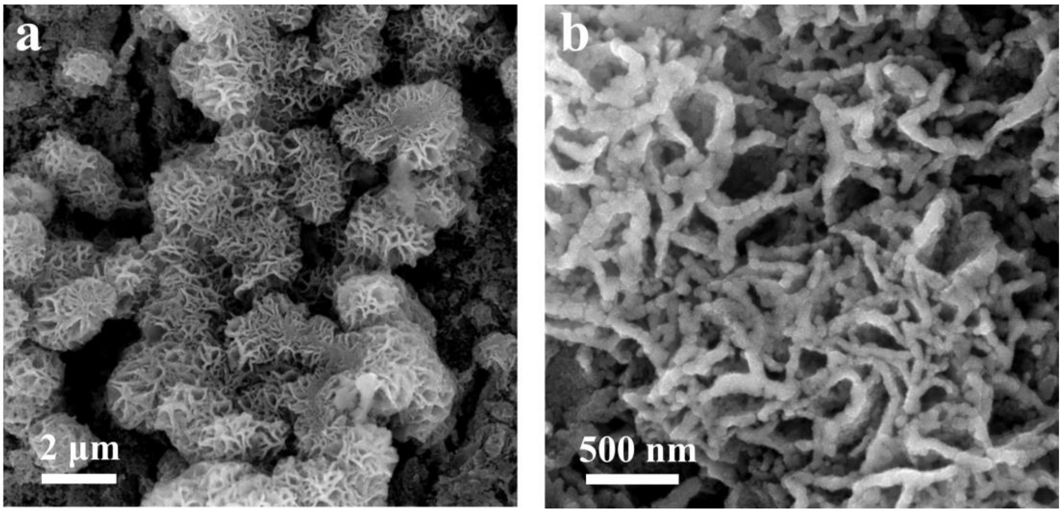

Figure S32. The morphology of Ni_3S_2/Co_9S_8/FeNiN catalyst after GOR catalysis.

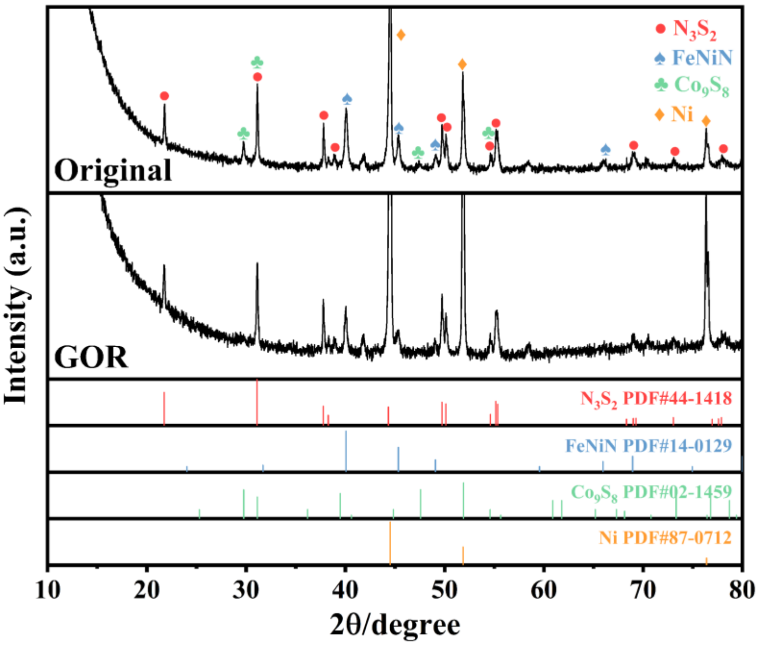

Figure S33. A typical XRD pattern of Ni_3S_2/Co_9S_8/FeNiN before and after GOR testing

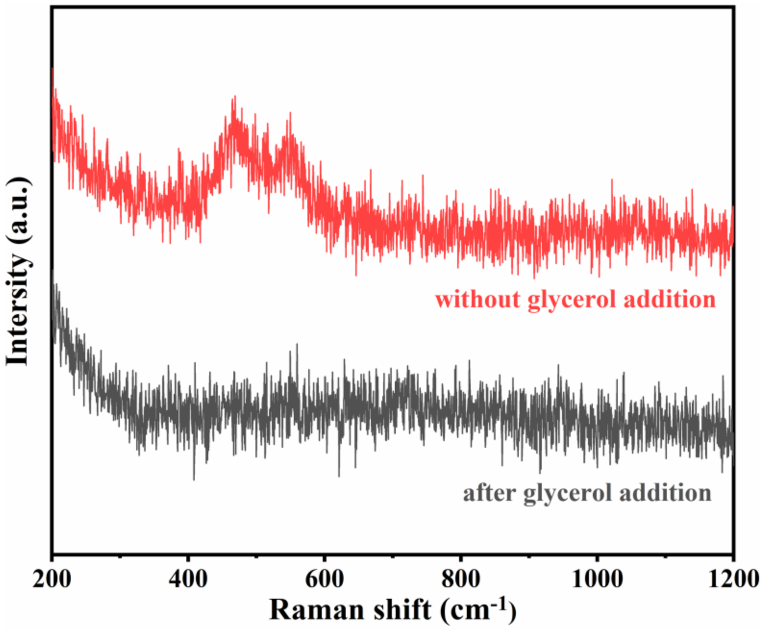

Figure S34. Raman spectra of Ni_3S_2/Co_9S_8/FeNiN catalyst tested at 1.374 V in 1 M KOH with and without glycerol addition.

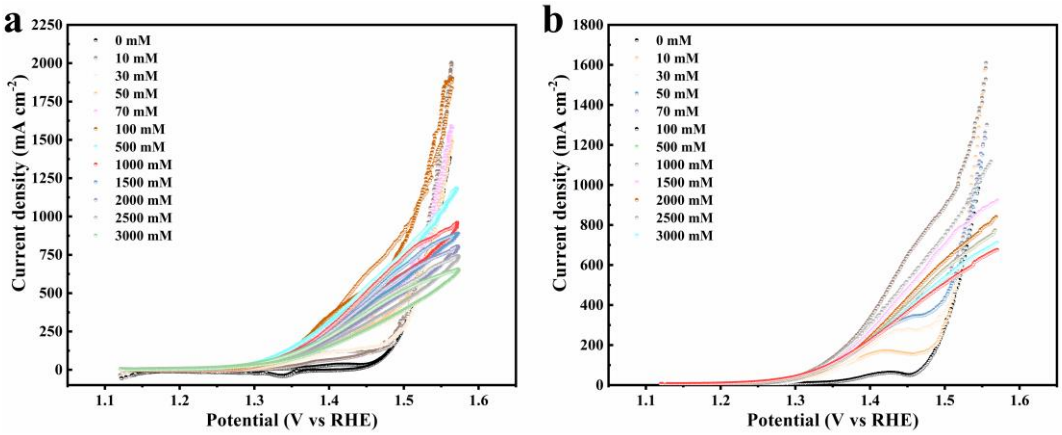

Figure S35. (a) Cyclic voltammetry curves and (b) linear polarization curves of Ni_3S_2/Co_9S_8/FeNiN catalyst in 1 M KOH with different glycerol concentrations at a scan rate of 1 mV s^{-1}.

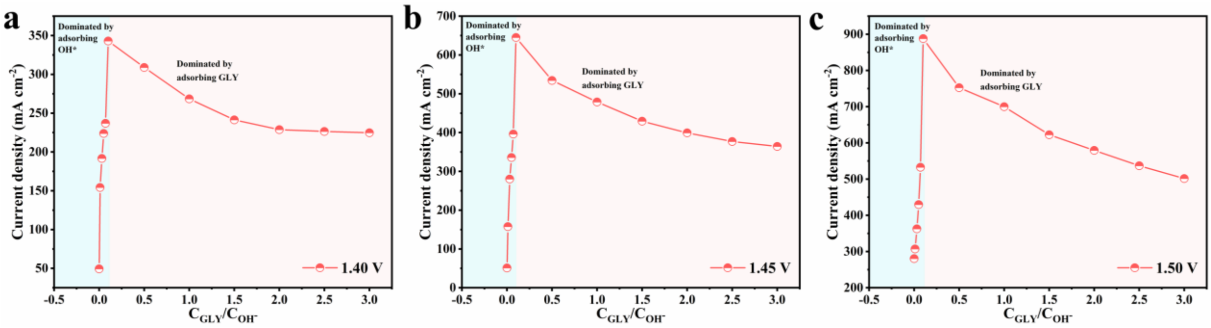

Figure S36. Relationship between the concentration ratio of glycerol to OH$^-$ and current density at potentials of (a) 1.40 V, (b) 1.45 V, and (c) 1.50 V.

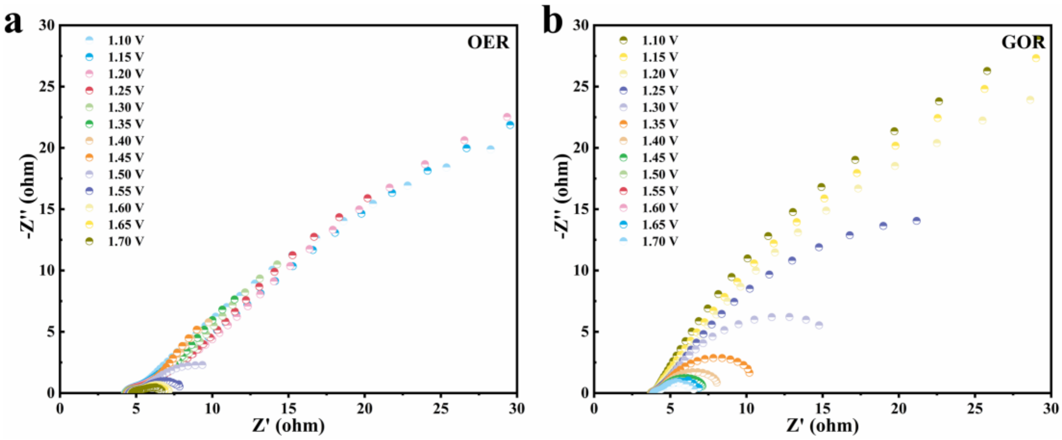

Figure S37. The Nyquist plots of $Ni_3S_2/Co_9S_8/FeNiN$ catalyst at different applied potentials in 1 M KOH (a) without glycerol and (b) with glycerol.

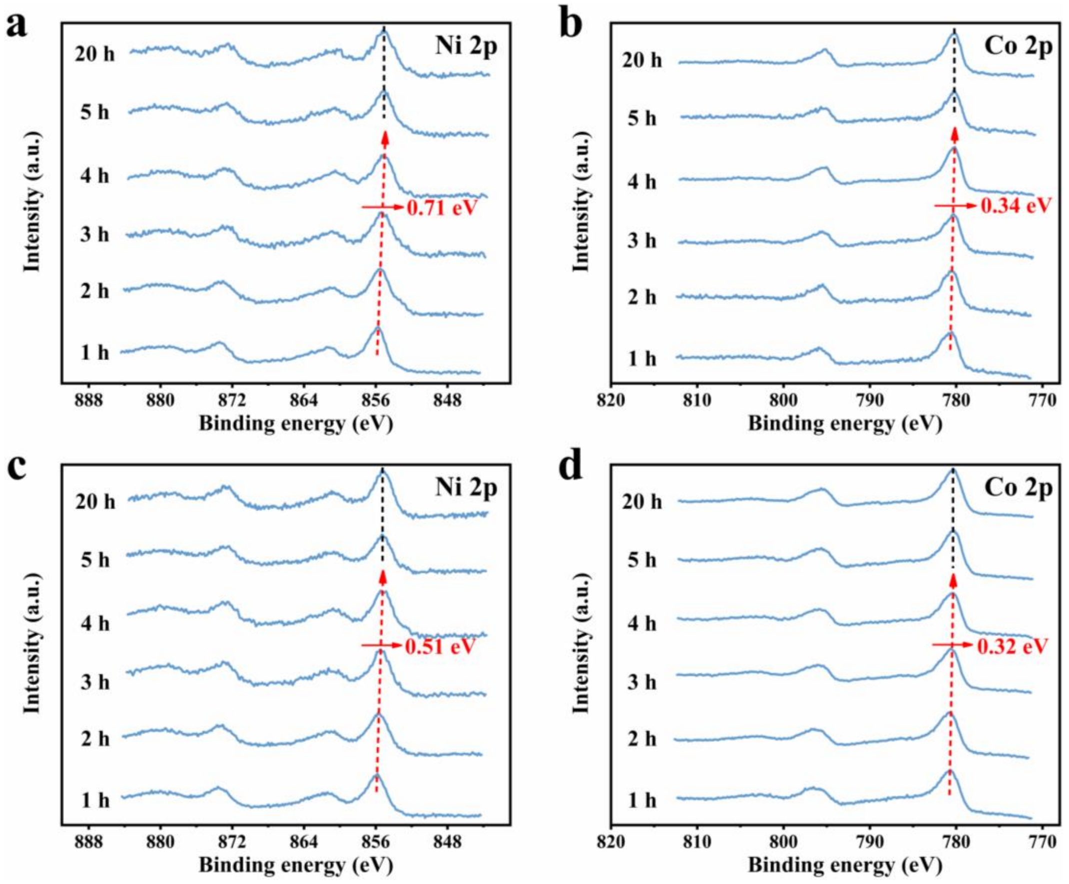

Figure S38. Operando XPS analysis of Ni $2p_{3/2}$ and Co $2p_{3/2}$ for Ni_3S_2/Co_9S_8/FeNiN catalyst tested at 1000 mA cm^{-2} for OER (a,b) or GOR (c,d).

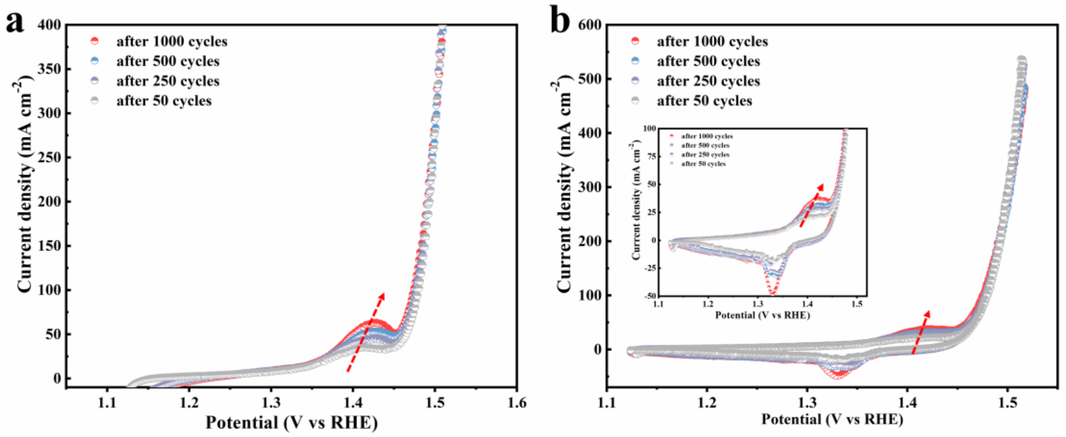

Figure S39. (a) The linear polarization curves recorded at a scan rate of 1 mV s^{-1} after different cycles. (b) Cyclic voltammetry curves recorded at a scan rate of 1 mV s^{-1} after different cycles, along with magnified local images.

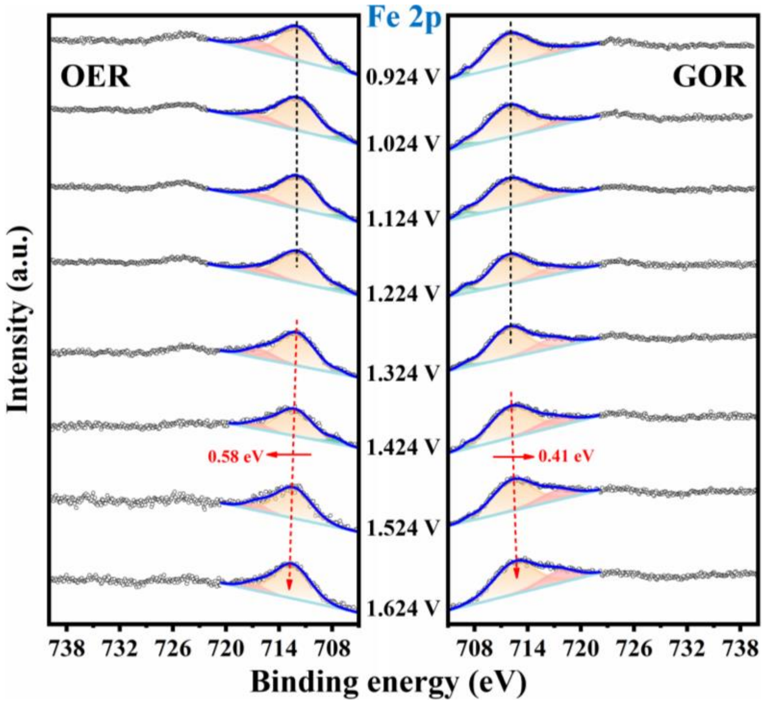

Figure S40. In situ Fe $2p_{3/2}$ XPS spectral analysis of $Ni_3S_2/Co_9S_8/FeNiN$ catalyst at different potentials in 1 M KOH with and without 0.1 M glycerol.

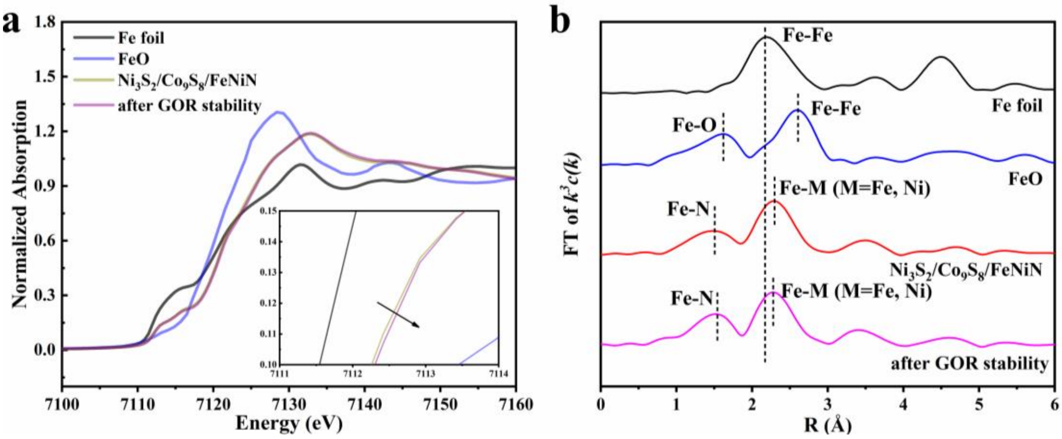

Figure S41. (a) Fe-K edge XANES spectra of $Ni_3S_2/Co_9S_8/FeNiN$ at different states. (b) Fe-K edge FT-EXAFS curves of $Ni_3S_2/Co_9S_8/FeNiN$ at different states.

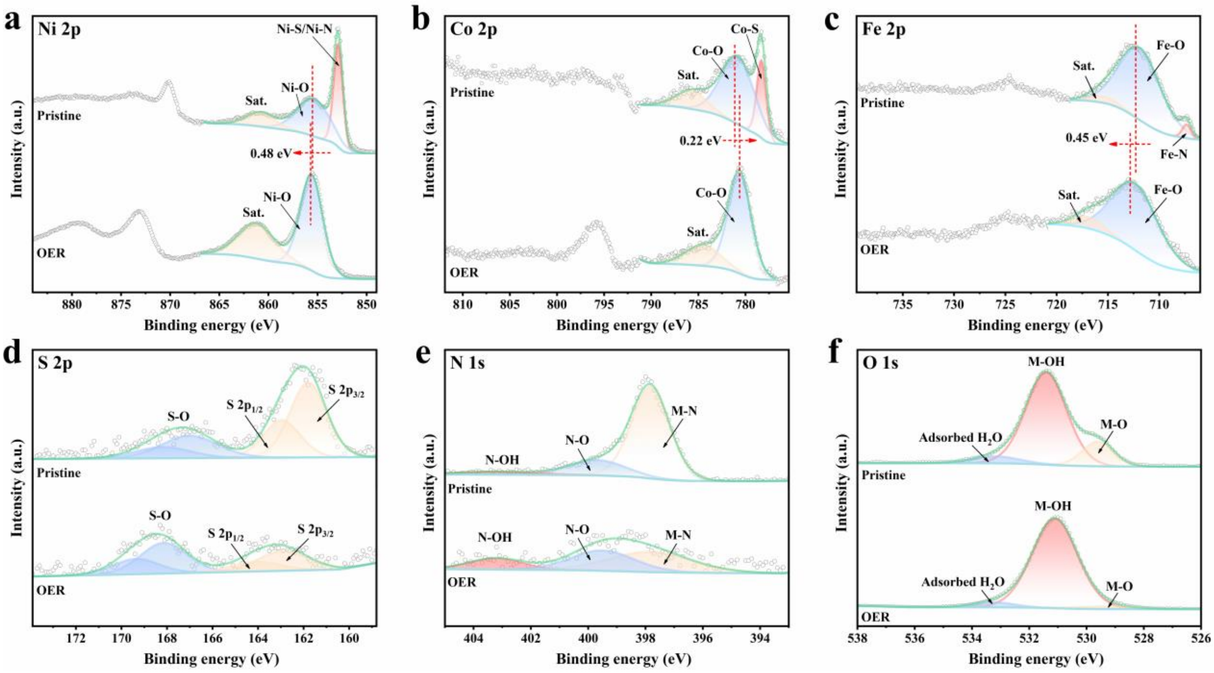

Figure S42. XPS spectra of Ni_3S_2/Co_9S_8/FeNiN after OER testing at 300 mA cm^{-2}: (a) Ni 2p, (b) Co 2p, (c) Fe 2p, (d) S 2p, (e) N 1s and (f) O 1s.

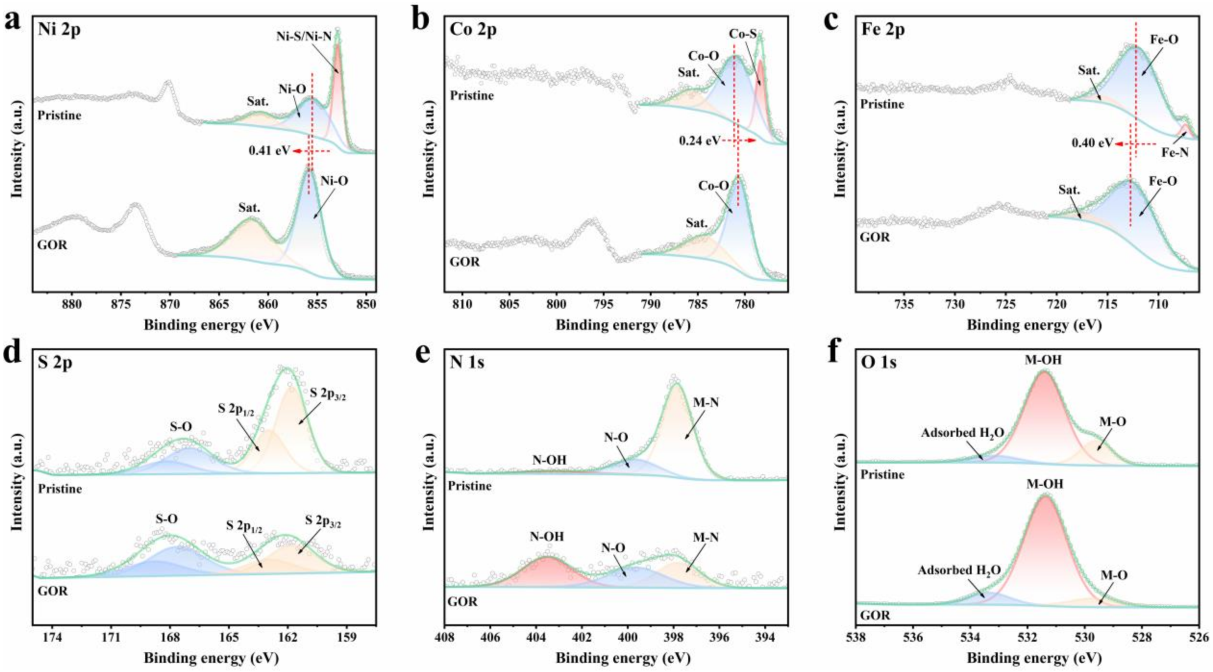

Figure S43. XPS spectra of Ni_3S_2/Co_9S_8/FeNiN after GOR testing at 100 mA cm^{-2}: (a) Ni 2p, (b) Co 2p, (c) Fe 2p, (d) S 2p, (e) N 1s and (f) O 1s.

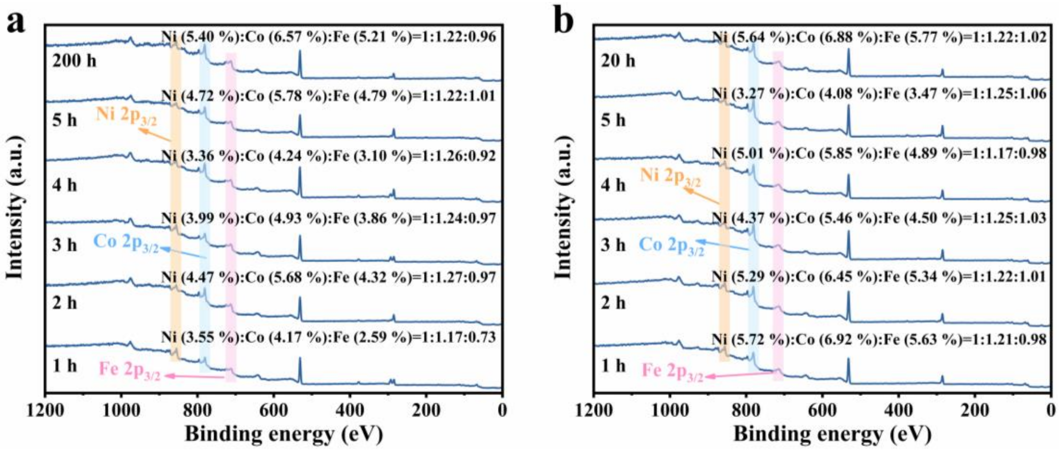

Figure S44. XPS survey spectra of post-OER (a) and post-GOR (b) catalysts after continuous operation at 1000 mA cm^{-2} for different times.

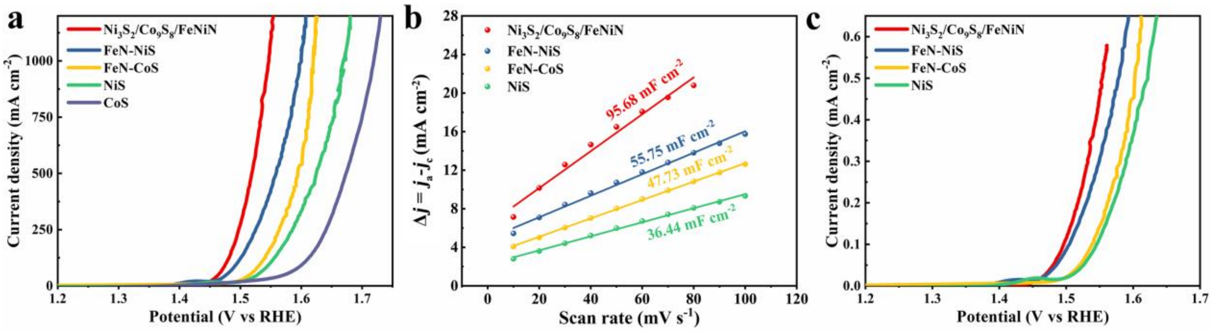

Figure S45. (a) The polarization curves of different electrocatalysts for the OER. (b) The double-layer capacitances (C_{dl}) of the electrocatalysts. (c) The electrochemical surface area (ECSA)-normalized polarization curves of these catalysts (ECSA=C_{dl}/C_s, C_s = 40 μF cm^{-2}). It is noted that Ni_3S_2/Co_9S_8/FeNiN has a current density comparable to FeN-NiS at the same potential, indicating that $Ni_{1-x}Fe_xOOH$ species may contribute more to the catalytic activity than CoOOH.

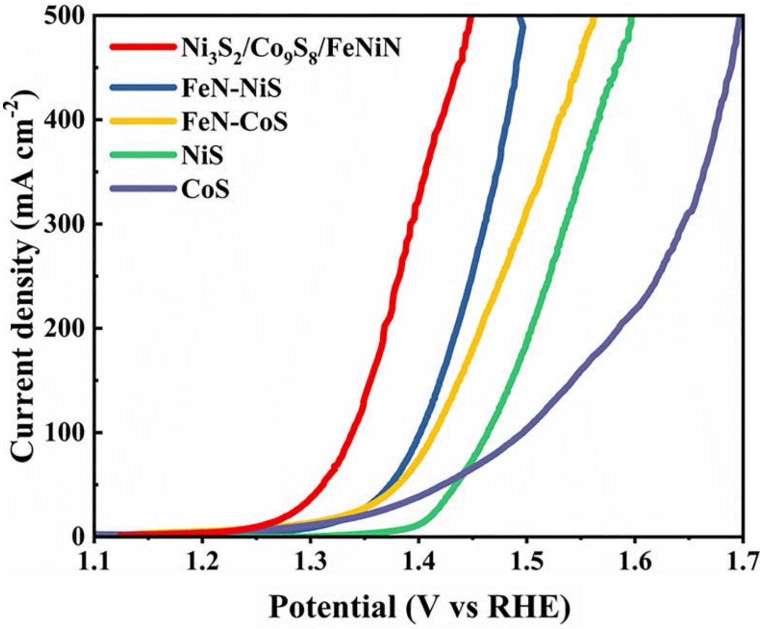

Figure S46. The GOR polarization curves of Ni_3S_2/Co_9S_8/FeNiN, FeN-NiS, FeN-CoS, NiS and CoS samples.

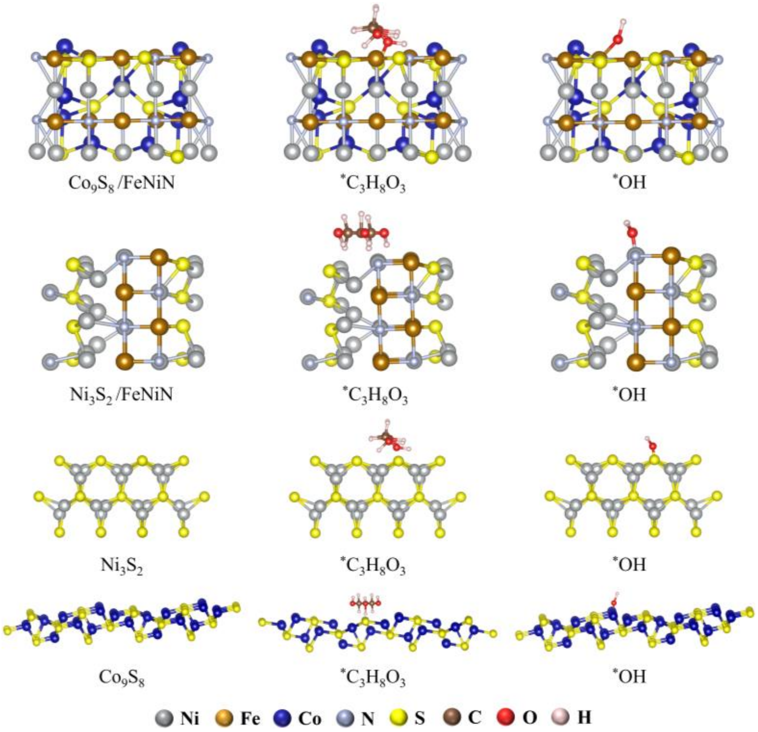

Figure S47. The optimized atomic configurations of Co_9S_8/FeNiN, Ni_3S_2/FeNiN, Ni_3S_2 and Co_9S_8 along with the corresponding adsorption configurations of $C_3H_8O_3$ and OH^-.

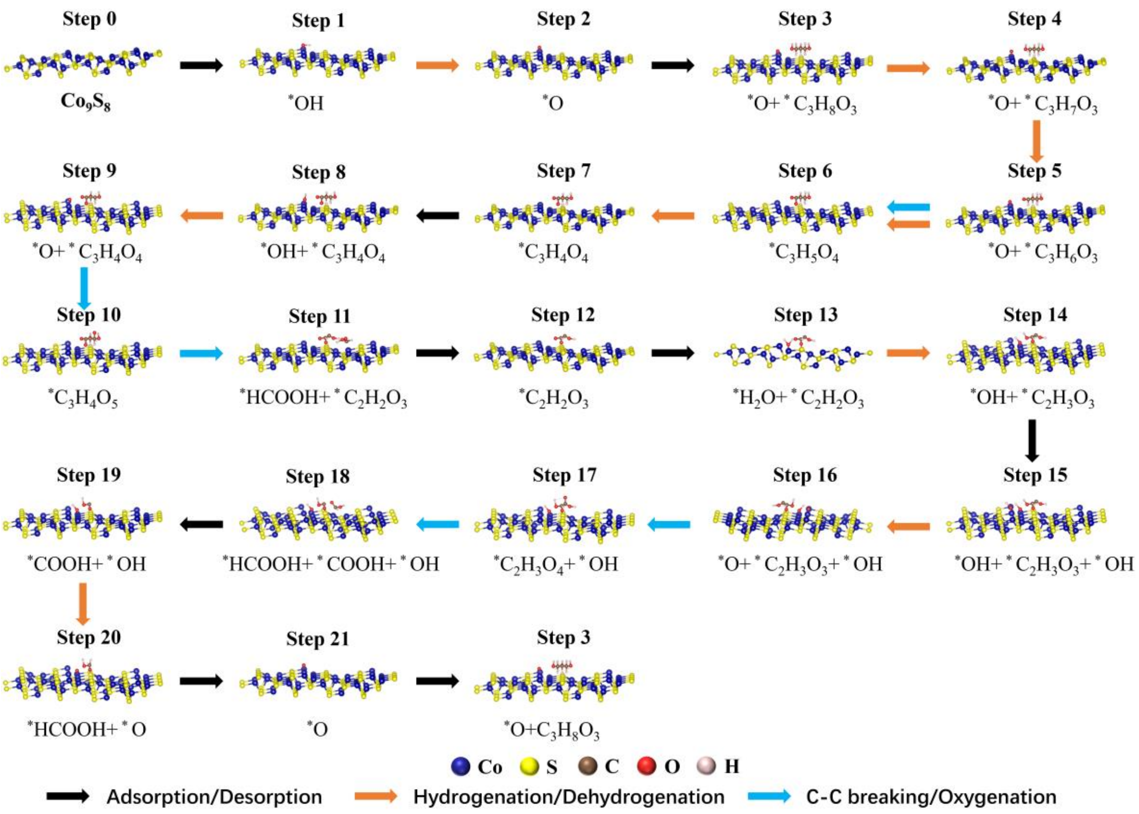

Figure S48. The complete pathway for the formation of formic acid from glycerol oxidation reaction, along with the atomic configurations on Co_9S_8.

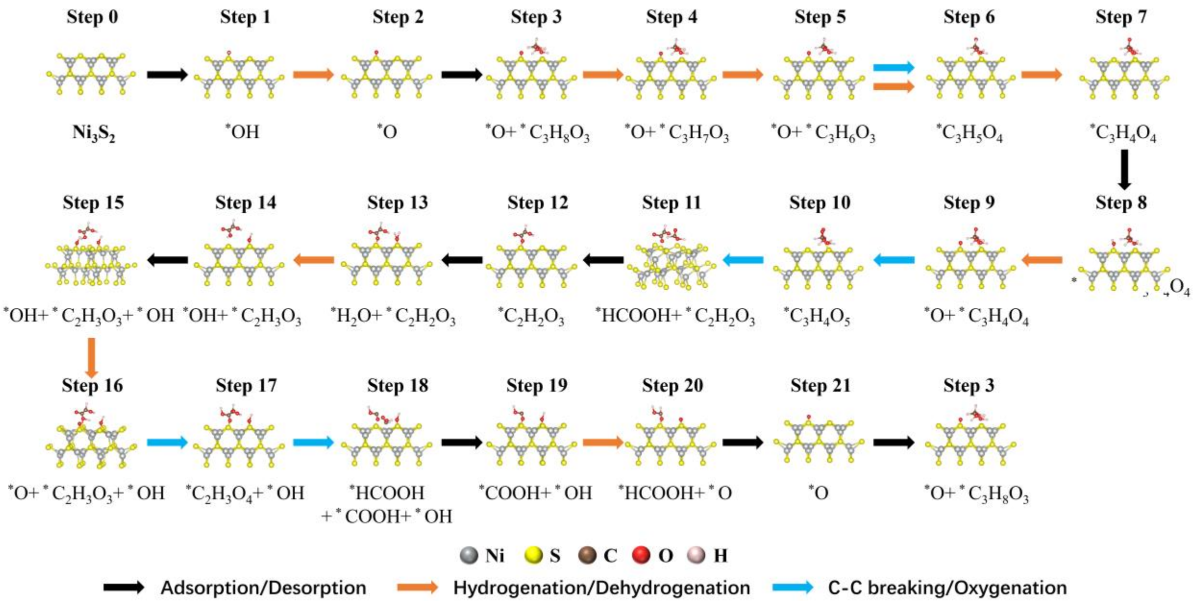

Figure S49. The complete pathway for the formation of formic acid from glycerol oxidation reaction, along with the atomic configurations on Ni_3S_2.

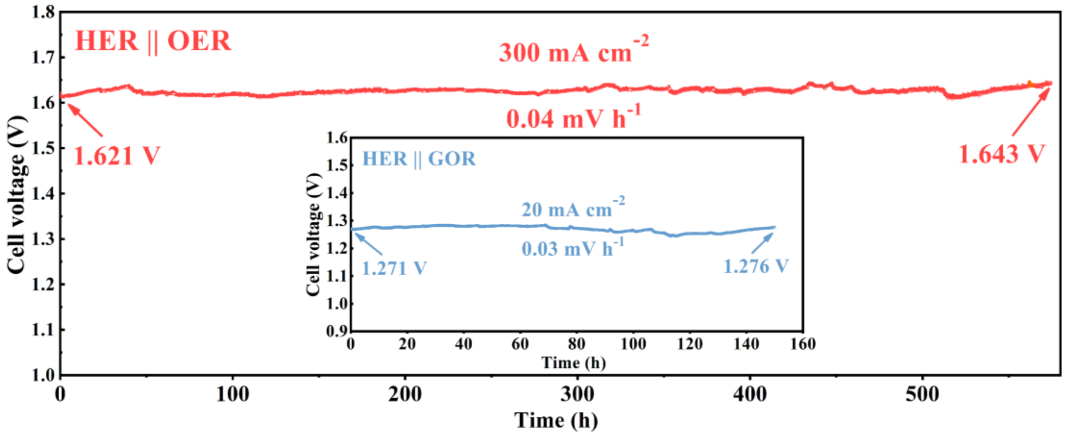

Figure S50. Durability tests for overall water electrolysis at 300 mA cm^{-2} and hybrid water electrolysis at 20 mA cm^{-2}.

Table S1. Comparison of the OER overpotentials required at 100 and 300 mA cm^{-2} among different transition metal-based electrocatalysts in 1 M KOH reported hitherto.

Catalyst	**Electrolyte**	**Overpotential at 100 mA cm^{-2}**	**Overpotential at 300 mA cm^{-2}**	**Ref.**
Ni_3S_2/Co_9S_8/FeNiN	1 M KOH	246 mV	272 mV	This work
NiFe-LDH/FeOOH	1 M KOH	236 mV	~275 mV	8
Ni_3S_2/Fe-NiP_x	1 M KOH	240 mV	~260 mV	9
Fe-CoP@Ni_2P	1 M KOH	~248 mV	~280 mV	10
NiFe LDH-PMo12	1 M KOH	249 mV	~285 mV	11
Fe-$Co(OH)_2/Fe_2O_3$	1 M KOH	249 mV	-	12
Ni_2P/FeP	1 M KOH	250 mV	~290 mV	13
$Fe_{0.9}Ni_{2.1}S_2$	1 M KOH	252 mV	~280 mV	14
$Ni_{0.3}Fe_{0.7}$-LDH	1 M KOH	256 mV	~282 mV	15
Ni_2P-Fe_2P	1 M KOH	261 mV	~295 mV	16
Cu_2S/CoFeCuOOH	1 M KOH	268 mV	~315 mV	17
Mo-Ni_3S_2/Ni_xP_y	1 M KOH	270 mV	~290 mV	18
Fe-doped-(Ni-MOFs)/FeOOH	1 M KOH	278 mV	303 mV	19
Fe-18 h	1 M KOH	279 mV	~300 mV	20
L-TA-FeNi CP	1 M KOH	280 mV	~340 mV	21
Fe-Ni_3S_2	1 M KOH	290 mV	~310 mV	22
Fe_2OF_4	1 M KOH	~290 mV	~350 mV	23
Ni_5Co_3Mo-OH	1 M KOH	304 mV	~318 mV	24
FeCoNiMnRu	1 M KOH	308 mV	~520 mV	25
Fe_2Co-MOF@M-OOH-ER	1 M KOH	360 mV	~620 mV	26
$Ni_xFe_{1-x}S$	1 M KOH	~370 mV	548 mV	27

Table S2. Comparison of the catalytic performance of this catalyst with other transition metal-based electrocatalysts for organic oxidation reactions reported recently.

Catalyst	Organics	Product	Potential at 100 mA cm^{-2}	Ref.
Ni_3S_2/Co_9S_8/FeNiN	1 M KOH + 0.1 M glycerol	formate	1.338 V	This work
$NiCo_2O_4$	1 M KOH + 0.1 M glycerol	formate	1.27 V	28
Ni_3N/Co_3N-NWs	1 M KOH + 0.1 M glycerol	formate	1.30 V	29
Ru@MnO_2	1 M KOH + 0.5 M glycerol	formate	1.52 V	30
CoNiCuMnMo NPs	5 mM H_2SO_4 + 0.2 M glycerol	formate	~1.34 V	31
MnO_2	1 M KOH + 0.1 M glycerol	formate	~1.71 V	32
Mn-$CoSe_2$	1 M KOH + 0.1 M glycerol	formate	~1.54 V	33
(CoNiCuMnMo)Se	1 M KOH + 0.1 M glycerol	formate	1.40 V	34
R–NiCuO	1 M KOH + 0.1 M glycerol	formate	~1.42 V	35
NiCo hydroxide	1 M KOH + 0.1 M glycerol	formate	1.35 V	36
Ni-WO_x	1 M KOH + 0.33 M urea	CO_2, N_2	1.40 V	37
O-NiMoP	5 M KOH + 0.5 M urea	CO_2, N_2	1.41 V	38
CoMn/$CoMn_2O_4$	1 M KOH + 0.5 M urea	CO_2, N_2	1.36 V	39
$Ni_2Fe(CN)_6$	1 M KOH + 0.33 M urea	CO_2, N_2	1.35 V	40
$Mn_{0.2}NiS$	1 M KOH + 100 mM HMF	FDCA	1.35 V	41
NiCoFe-LDHs	1 M NaOH + 10 mM HMF	FDCA	~1.75 V	42
$Ni(OH)_2$/NiFeP	1 M KOH + 10 mM HMF	FDCA	~1.43 V	43
Pd/NiCo	1 M KOH + 50 mM HMF	FDCA	~1.69 V	44
Vo-Co_3O_4	1 M KOH + 50 mM HMF	FDCA	~1.54 V	45
Fe-NF-500	1 M KOH + 1 M MeOH	formate	1.39 V	46
Mo-Co_4N	1 M KOH + 3 M MeOH	formate	1.48 V	47
$Ni(OH)_2$	1 M KOH + 0.5 M MeOH	formate	1.36 V	48

Table S3. Comparison of the overall electrolysis performance among glycerol hybrid water electrolyzers reported recently.

Catalyst	Organics	Product	Voltage for 100 mA cm^{-2}	Voltage for 400 mA cm^{-2}	Ref.
$Ni_3S_2/Co_9S_8/FeNiN^{(+)}$‖ $NiMoN^{(-)}$	1 M KOH + 0.1 M glycerol	formate	1.386 V	1.491 V	This work
$NiCo_2O_4^{(+)}$‖$Pt/C^{(-)}$	1 M KOH + 0.1 M glycerol	formate	1.45 V	1.98 V	28
$Ru@MnO_{2-x}^{(+/-)}$	1 M KOH + 0.5 M glycerol	formate	1.35 V	~1.63 V	30
NiCo hydroxide$^{(+/-)}$	1 M KOH + 0.1 M glycerol	formate	1.58 V	-	36
Ni_3N/Co_3N-NWs$^{(+/-)}$	1 M KOH + 0.1 M glycerol	formate	1.59 V	2.04 V	29
NiVRu-LDHs$^{(+/-)}$	1 M KOH + 0.1 M glycerol	formate	1.62 V	1.85 V	49
$NiO^{(+)}$‖$NiMoNH^{(-)}$	1 M KOH + 0.1 M glycerol	formate	1.54 V	~1.92 V	50
NC/Ni-Mo-N$^{(+/-)}$	1 M KOH + 0.1 M glycerol	formate	~1.58 V	~1.68 V	51
NiCrO-VCr,O$^{(+)}$‖$Ni^{(-)}$	1 M KOH + 0.1 M glycerol	formate	~1.68 V	2.50 V	52
MnCoN@C$^{(+/-)}$	1 M KOH + 0.3 M glycerol	formate	1.51	1.69 V	53
Ni-Mo-N$^{(+/-)}$	1 M KOH + 0.1 M glycerol	formate	~1.78 V	-	54

Table S4. Comparison of the overall electrolysis performance with other recently reported electrolyzers in alkaline electrolyte.

Catalyst	Electrolyte	Voltage for 100 mA cm^{-2}	Voltage for 500 mA cm^{-2}	Ref.
$Ni_3S_2/Co_9S_8/FeNiN^{(+)}$‖$NiMoN^{(-)}$	1 M KOH	1.557 V	1.662 V	This work
$(Ni,Fe)OOH^{(+)}$‖$MoNi4^{(-)}$	1 M KOH	1.491 V	1.586 V	55
$Fe_4N/Co_3N@MoO_2^{(+/-)}$	1 M KOH	1.520 V	1.59 V	56
$NiMoN/NiFe^{(+/-)}$	1 M KOH	~1.53 V	1.70 V	57
$FeP/Ni_2P^{(+/-)}$	1 M KOH	1.682 V	1.865 V	58
NFM-$OV_R^{(+/-)}$	1 M KOH	~1.65 V	1.74 V	59
$Fe_2P/Ni_{1.5}Co_{1.5}N/Ni_2P^{(+/-)}$	1 M KOH	1.569 V	1.67 V	60
Fe-$Ni_3S_2^{(+/-)}$	1 M KOH	1.76 V	~1.92 V	22
$NiMoN/Ni_3S_2^{(+/-)}$	1 M KOH	1.63 V	1.85 V	61
$Ni(OH)_2^{(+)}$‖$Ru^{(-)}$	1 M KOH	1.639 V	1.82 V	62
$NiMoO_x/NiMoS^{(+/-)}$	1 M KOH	1.63 V	1.75 V	63

References

1. P. Giannozzi, O. Andreussi, T. Brumme, O. Bunau, M. B. Nardelli, M. Calandra, R. Car, C. Cavazzoni, D. Ceresoli and M. Cococcioni, *J. Phys.: Condens. Matter.*, 2017, **29**, 465901.
2. P. Giannozzi, S. Baroni, N. Bonini, M. Calandra, R. Car, C. Cavazzoni, D. Ceresoli, G. L. Chiarotti, M. Cococcioni and I. Dabo, *J. Phys.: Condens. Matter.*, 2009, **21**, 395502.
3. J. Paier, R. Hirschl, M. Marsman and G. Kresse, *J. Chem. Phys.*, 2005, **122**, 234102.
4. P. John, K. B. Perdew and E. Matthias, *Phys. Rev. Lett.*, 1996, **77**, 3865.
5. P. E. Blochl, *Phys. Rev. B*, 1994, **50**, 17953-17979.
6. S. Grimme, S. Ehrlich and L. Goerigk, *J. Comput. Chem.*, 2011, **32**, 1456-1465.
7. S. Grimme, J. Antony, S. Ehrlich and H. Krieg, *J. Chem. Phys.*, 2010, **132**, 154104.
8. Y. H. Wang, L. Li, J. Shi, M. Y. Xie, J. Nie, G. F. Huang, B. Li, W. Hu, A. Pan and W. Q. Huang, *Adv. Sci.*, 2023, **10**, 2303321.
9. X. Luo, P. Ji, P. Wang, X. Tan, L. Chen and S. Mu, *Adv. Sci*., 2022, **9**, 2104846.
10. Z. Duan, D. Zhao, Y. Sun, X. Tan and X. Wu, *Nano Res.*, 2022, **15**, 8865-8871.
11. Z. Cai, P. Wang, J. Zhang, A. Chen, J. Zhang, Y. Yan and X. Wang, *Adv. Mater.*, 2022, **34**, 2110696.
12. S. Xin, Y. Tang, B. Jia, Z. Zhang, C. Li, R. Bao, C. Li, J. Yi, J. Wang and T. Ma, *Adv. Funct. Mater.*, 2023, **33**, 2305243.
13. M. Jiang, H. Zhai, L. Chen, L. Mei, P. Tan, K. Yang and J. Pan, *Adv. Funct. Mater.*, 2023, **33**, 2302621.
14. B. Fei, Z. Chen, J. Liu, H. Xu, X. Yan, H. Qing, M. Chen and R. Wu, *Adv. Energy Mater.*, 2020, **10**, 2001963.
15. Y. Zhai, X. Ren, Y. Sun, D. Li, B. Wang and S. Liu, *Appl. Catal. B*, 2023, **323**, 122091.

16. L. B. Wu, L. Yu, F. H. Zhang, B. McElhenny, D. Luo, A. Karim, S. Chen and Z. F. Ren, *Adv. Funct. Mater.*, 2021, **31**, 2006484.

17. C. Wang, P. Zhai, M. Xia, W. Liu, J. Gao, L. Sun and J. Hou, *Adv. Mater.*, 2023, **35**, 2209307.

18. X. Luo, P. Ji, P. Wang, R. Cheng, D. Chen, C. Lin, J. Zhang, J. He, Z. Shi, N. Li, S. Xiao and S. Mu, *Adv. Energy Mater.*, 2020, **10**, 1903891.

19. C. F. Li, L. J. Xie, J. W. Zhao, L. F. Gu, H. B. Tang, L. Zheng and G. R. Li, *Angew. Chem. Int. Ed.*, 2022, **61**, e202116934.

20. N. K. Shrestha, S. A. Patil, J. Han, S. Cho, A. I. Inamdar, H. Kim and H. Im, *J. Mater. Chem. A*, 2022, **10**, 8989-9000.

21. T. Feng, W. Chen, J. Xue, F. Cao, Z. Chen, J. Ye, C. Xiao and H. Lu, *Adv. Funct. Mater.*, 2023, **33**, 2215051.

22. D. Li, W. Wan, Z. Wang, H. Wu, S. Wu, T. Jiang, G. Cai, C. Jiang and F. Ren, *Adv. Energy Mater.*, 2022, **12**, 2201913.

23. G. Zhang, Z. Li, J. Zeng, L. Yu, C. Zuo, P. Wen, Y. Liu, L. Zhong, H. Chen and Y. Qiu, *Appl. Catal. B*, 2022, **319**, 121921.

24. S. Hao, L. Chen, C. Yu, B. Yang, Z. Li, Y. Hou, L. Lei and X. Zhang, *ACS Energy Lett.*, 2019, **4**, 952-959.

25. J. Hao, Z. Zhuang, K. Cao, G. Gao, C. Wang, F. Lai, S. Lu, P. Ma, W. Dong, T. Liu, M. Du and H. Zhu, *Nat. Commun.*, 2022, **13**, 2662.

26. Z. K. Shi, Z. B. Yu, R. H. Jiang, J. Huang, Y. P. Hou, J. H. Chen, Y. Q. Zhang, H. X. Zhu, B. Wang and H. Pang, *J. Mater. Chem. A*, 2021, **9**, 11415-11426.

27. Q. Han, Y. Luo, J. Li, X. Du, S. Sun, Y. Wang, G. Liu and Z. Chen, *Appl. Catal. B*, 2022,

304, 120937.

28. W. Luo, H. Tian, Q. Li, G. Meng, Z. Chang, C. Chen, R. Shen, X. Yu, L. Zhu, F. Kong, X. Cui and J. Shi, *Adv. Funct. Mater.*, 2024, **34**, 2306995.
29. Y. Zhu, Q. Qian, Y. Chen, X. He, X. Shi, W. Wang, Z. Li, Y. Feng, G. Zhang and F. Cheng, *Adv. Funct. Mater.*, 2023, **33**, 2300547.
30. H. Yu, M. Hu, C. Chen, C. Hu, Q. Li, F. Hu, S. Peng and J. Ma, *Angew. Chem. Int. Ed.*, 2023, **62**, e202314569.
31. L. Fan, Y. Ji, G. Wang, J. Chen, K. Chen, X. Liu and Z. Wen, *J. Am. Chem. Soc.*, 2022, **144**, 7224-7235.
32. Y. Li, X. Wei, S. Han, L. Chen and J. Shi, *Angew. Chem. Int. Ed.*, 2021, **60**, 21464-21472.
33. L. Fan, Y. Ji, G. Wang, Z. Zhang, L. Yi, K. Chen, X. Liu and Z. Wen, *J. Energy Chem.*, 2022, **72**, 424-431.
34. H. Yao, Y. Wang, Y. Zheng, X. Yu, J. Ge, Y. Zhu and X. Guo, *Nano Res.*, 2023, **16**, 10832-10839.
35. S. Li, P. Ma, C. Gao, L. Liu, X. Wang, M. Shakouri, R. Chernikov, K. Wang, D. Liu, R. Ma and J. Wang, *Energy Environ. Sci.*, 2022, **15**, 3004-3014.
36. Z. He, J. Hwang, Z. Gong, M. Zhou, N. Zhang, X. Kang, J. W. Han and Y. Chen, *Nat Commun.*, 2022, **13**, 3777.
37. L. Wang, Y. Zhu, Y. Wen, S. Li, C. Cui, F. Ni, Y. Liu, H. Lin, Y. Li, H. Peng and B. Zhang, *Angew. Chem. Int. Ed.*, 2021, **60**, 10577-10582.
38. H. Jiang, M. Z. Sun, S. L. Wu, B. L. Huang, C. S. Lee and W. J. Zhang, *Adv. Funct. Mater.*, 2021, **31**, 2104951.
39. C. Wang, H. Lu, Z. Mao, C. Yan, G. Shen and X. Wang, *Adv. Funct. Mater.*, 2020, **30**,

2000556.

40. S. K. Geng, Y. Zheng, S. Q. Li, H. Su, X. Zhao, J. Hu, H. B. Shu, M. Jaroniec, P. Chen, Q. H. Liu and S. Z. Qiao, *Nat. Energy*, 2021, **6**, 904-912.
41. S. Li, S. Wang, Y. Wang, J. He, K. Li, Y. Xu, M. Wang, S. Zhao, X. Li, X. Zhong and J. Wang, *Adv. Funct. Mater.*, 2023, **33**, 2214488.
42. M. Zhang, Y. Liu, B. Liu, Z. Chen, H. Xu and K. Yan, *ACS Catal.*, 2020, **10**, 5179-5189.
43. R. Luo, Y. Li, L. Xing, N. Wang, R. Zhong, Z. Qian, C. Du, G. Yin, Y. Wang and L. Du, *Appl. Catal. B*, 2022, **311**, 121357.
44. G. Liu, T. Nie, Z. Song, X. Sun, T. Shen, S. Bai, L. Zheng and Y. F. Song, *Angew. Chem. Int. Ed.*, 2023, **62**, e202311696.
45. Y. Lu, T. Liu, C. L. Dong, C. Yang, L. Zhou, Y. C. Huang, Y. Li, B. Zhou, Y. Zou and S. Wang, *Adv. Mater.*, 2022, **34**, 2107185.
46. Y. Hao, D. Yu, S. Zhu, C. H. Kuo, Y. M. Chang, L. Wang, H. Y. Chen, M. Shao and S. Peng, *Energy Environ. Sci.*, 2023, **16**, 1100-1110.
47. T. Wang, X. Cao, H. Qin, X. Chen, J. Li and L. Jiao, *J. Mater. Chem. A.*, 2021, **9**, 21094-21100.
48. J. Hao, J. Liu, D. Wu, M. Chen, Y. Liang, Q. Wang, L. Wang, X. Z. Fu and J. L. Luo, *Appl. Catal. B*, 2021, **281**, 119510.
49. Q. Qian, X. He, Z. Li, Y. Chen, Y. Feng, M. Cheng, H. Zhang, W. Wang, C. Xiao, G. Zhang and Y. Xie, *Adv. Mater.*, 2023, **35**, 2300935.
50. S. Li, D. Liu, G. Wang, P. Ma, X. Wang, J. Wang and R. Ma, *Nano-Micro Lett.*, 2023, **15**, 189.
51. Y. Xu, M. Liu, S. Wang, K. Ren, M. Wang, Z. Wang, X. Li, L. Wang and H. Wang, *Appl.*

Catal. B, 2021, **298**, 120493.

52. Z. Xia, C. Ma, Y. Fan, Y. Lu, Y. C. Huang, Y. Pan, Y. Wu, Q. Luo, Y. He, C. L. Dong, S. Wang and Y. Zou, *ACS Catal.*, 2024, **14**, 1930-1938.
53. J. Li, X. Meng, X. Song, J. Qi, F. Liu, X. Xiao, Y. Du, G. Xu, Z. Jiang, S. Ye, S. Huang and J. Qiu, *Adv. Funct. Mater.*, 2024, **34**, 2316718.
54. Y. Li, X. Wei, L. Chen, J. Shi and M. He, *Nat. Commun.*, 2019, **10**, 5335.
55. H. Zhou, F. Yu, Q. Zhu, J. Sun, F. Qin, L. Yu, J. Bao, Y. Yu, S. Chen and Z. Ren, *Energy Environ. Sci.*, 2018, **11**, 2858-2864.
56. L. Liao, D. Li, Y. Zhang, Y. Zhang, F. Yu, L. Yang, X. Wang, D. Tang and H. Zhou, *Adv. Mater.*, 2024, **36**, 2405852.
57. P. Zhai, C. Wang, Y. Zhao, Y. Zhang, J. Gao, Li. Sun and J. Hou, *Nat Commun.*, 2023, **14**, 1873.
58. F. Yu, H. Zhou, Y. Huang, J. Sun, F. Qin, J. Bao, W. A. G. III, S. Chen and Z. Ren, *Nat Commun.*, 2018, **9**, 2551.
59. L. Xiao, C. Cheng, T. Yang, J. Zhang, Y. Han, C. Han, W. Lv, H. Tan, X. Zhao, P. Yin, C. Dong, H. Liu, X. Du and J. Yang, *Adv. Mater.*, 2024, **36**, 2411134.
60. F. Zhang, Y. Liu, F. Yu, H. Pang, X. Zhou, D. Li, W. Ma, Q. Zhou, Y. Mo and H. Zhou, *ACS Nano*, 2023, **17**, 1681-1692.
61. L. L. Ma, Y.-R. Hao, J. Sun, Y. Chen, C. Li, H. Xue, J. Sun, Q. Wang and L. Wu, *Adv. Funct. Mater.*, 2024, 2409924.
62. Z. Gong, P. Chen, H. Gong, K. Huang, G. Ye and H. Fei, *Adv. Mater.*, 2024, **36**, 2409292.
63. P. Zhai, Y. Zhang, Y. Wu, J. Gao, B. Zhang, S. Cao, Y. Zhang, Z. Li, L. Sun and J. Hou, *Nat Commun.*, 2020, **11**, 5462.